Biophysical Journal (2022) **121** (In Press) https://doi.org/10.1016/j.bpj.2022.10.033
https://authors.elsevier.com/a/1g2%7E61SPT0Fg8

Close agreement between deterministic vs. stochastic modeling of first-passage time to vesicle fusion

Victor V. Matveev

Department of Mathematical Sciences, New Jersey Institute of Technology, Newark, NJ USA 07102

matveev@njit.edu http://web.njit.edu/~matveev

Running title: **Modeling waiting time to vesicle fusion**

Abstract

Ca^{2+}-dependent cell processes such as neurotransmitter or endocrine vesicle fusion are inherently stochastic due to large fluctuations in Ca^{2+} channel gating, Ca^{2+} diffusion and Ca^{2+} binding to buffers and target sensors. However, prior studies revealed closer-than-expected agreement between deterministic and stochastic simulations of Ca^{2+} diffusion, buffering and sensing, as long as Ca^{2+} channel gating is not Ca^{2+}-dependent. To understand this result more fully, we present a comparative study complementing prior work, focusing on Ca^{2+} dynamics downstream of Ca^{2+} channel gating. Specifically, we compare deterministic (mean-field / mass-action) and stochastic simulations of vesicle exocytosis latency, quantified by the probability density of the first-passage time (FPT) to the Ca^{2+}-bound state of a vesicle fusion sensor, following a brief Ca^{2+} current pulse. We show that under physiological constraints, the discrepancy between FPT densities obtained using the two approaches remains small even if as few as ~50 Ca^{2+} ions enter per single channel-vesicle release unit. Using a reduced two-compartment model for ease of analysis, we illustrate how this close agreement arises from the smallness of *correlations* between fluctuations of the reactant molecule numbers, despite the large magnitude of the fluctuation *amplitudes*. This holds if all relevant reactions are *heteroreaction* between molecules of different species, as is the case for the bimolecular Ca^{2+} binding to buffers and downstream sensor targets. In this case diffusion and buffering effectively decorrelate the state of the Ca^{2+} sensor from local Ca^{2+} fluctuations. Thus, fluctuations in the Ca^{2+} sensor's state underlying the FPT distribution are only weakly affected by the fluctuations in the local Ca^{2+} concentration around its average, deterministically computable value.

Statement of Significance

Many fundamental Ca^{2+}-dependent cell processes are triggered by local Ca^{2+} elevations involving only a few hundred Ca^{2+} ions. Therefore, one expects large Ca^{2+} concentration fluctuations, which are ignored by deterministic reaction-diffusion modeling approaches. However, more accurate stochastic approaches require tracking trajectories of individual Ca^{2+} ions and its binding targets, which is very computationally expensive. This study reveals conditions under which Ca^{2+}-dependent processes like secretory vesicle fusion can be modeled using efficient deterministic approaches, without sacrificing significant accuracy. We find that deterministic methods can accurately predict the delay to the fusion of a neurotransmitter-containing vesicle, as long as the number of Ca^{2+} ions is above about 50. We reveal factors that explain the limited impact of stochastic fluctuations in this case.

I. INTRODUCTION

Many fundamental cell processes such as myocyte contraction and synaptic and endocrine secretory vesicle fusion are controlled by highly localized Ca^{2+} signals resulting from the opening of transmembrane Ca^{2+} channels (1-5). Imaging local Ca^{2+} concentration required for the study of these processes is a great challenge due to physical limitations on the spatial and temporal resolution of optical imaging, and necessarily perturb the Ca^{2+} signals being measured. Therefore, Ca^{2+} modeling continues to play a crucial role in the study of a variety of Ca^{2+}-dependent cell mechanisms. The main decision facing a modeler is whether to choose a deterministic or a stochastic solver (5-10). While deterministic mass-action reaction-diffusion approach offers superior computational efficiency, it completely ignores local fluctuations in Ca^{2+} resulting from the stochastic Ca^{2+} channel gating, diffusion, and biochemical reactions. For processes controlled by single-channel Ca^{2+} domains, fluctuations are considerable: a typical Ca^{2+} current of 0.2 pA and duration of 0.2 ms translates to an influx of only about 120 Ca^{2+} ions, many of which become bound to mobile buffers and transmembrane proteins before reaching their downstream target sensors (11-13). Thus, one should expect large Ca^{2+} concentration fluctuations at the location of a relevant Ca^{2+} sensor that only a few Ca^{2+} ions will reach (13,14). Stochastic fluctuations were shown to have functional consequences in reaction-diffusion models of a variety of cell processes (see e.g. (15-18)). For Ca^{2+}-controlled processes, such stochastic effects are especially pronounced in the presence of Ca^{2+}–induced Ca^{2+} release (CICR) responsible for excitation-contraction coupling in myocytes, since CICR introduces a direct feedback between Ca^{2+} fluctuations and Ca^{2+} influx (19-28).

Despite the widely recognized importance of stochastic effects, comparative studies suggest that downstream of stochastic channel gating, the discrepancy between deterministic and stochastic simulations of Ca^{2+} diffusion, buffering and binding can be surprisingly small (24,29). Therefore, in the absence of CICR, computationally inexpensive simulations of Markovian stochastic channel gating can be combined with deterministic models of Ca^{2+} diffusion and binding (either compartment-based or spatially resolved), leading to computationally inexpensive methods that avoid simulations of particle-based Brownian motion and stochastic reactions (7,27-30). This in fact has often been the approach even in the modeling of CICR, where Ca^{2+} channel gating is the primary source of fluctuations (5,19-21,31-39). This simplified approach has also proved useful in the study of vesicle fusion (40,41), Ca^{2+} signaling in dendrites (42), and Ca^{2+}-dependent K^+ channels (43).

Despite a large number of relevant studies, in particular a comprehensive comparative computational study by Modchang et al. (29), a deep understanding of the discrepancy between stochastic and deterministic simulations downstream of stochastic Ca^{2+} channel gating effects is still lacking. As a result, as has been noted previously (24), the choice between deterministic and stochastic solvers is usually made on a completely *ad hoc* basis. In particular, it is widely accepted that deterministic reaction-diffusion methods are highly inaccurate in the modeling of any biochemical process involving a small number of molecules (e.g. the number of Ca^{2+} ions, N_{Ca}). This expected inaccuracy is due to the well-known discrepancy between mass-action and stochastic representations of any nonlinear process (44,45).

However, here we show that the size of this discrepancy between deterministic and stochastic approaches is not always as large as expected from an often-used naïve $1/\sqrt{N_{Ca}}$ scaling, and depends not only on the size of the Ca^{2+} fluctuations, but also on the type of observable targeted by the modeling, and the type of reactions involved. In particular, following several recent studies, we focus on the first passage time distribution (FPTD) to full finding of a model Ca^{2+} sensor for vesicle fusion in the presence of bimolecular Ca^{2+} buffering reactions (13,14,46-51). We consider a maximally reduced but spatially resolved model that contain only two sources of fluctuations: (1) the diffusive fluctuations in Ca^{2+} concentration, and (2) the fluctuations due to Ca^{2+} binding and unbinding to Ca^{2+} buffers and sensors. Considering such a reduced

model reveals more clearly the interplay between fluctuations due to diffusion and reaction in limiting the accuracy of the mean-field modeling of Ca^{2+} sensor binding time. Our main finding is that the discrepancy between deterministic and stochastic estimates of FPTD can be negligible as long as the number of Ca^{2+} ions is above about ~50. Finally, to clarify our conclusions, we will also analyze an even simpler two-compartment model of Ca^{2+} diffusion and binding, following the approach of G.D. Smith and S.H. Weinberg (26,48,52). Our results further elucidate how the interplay between the diffusion and the reaction time scales affects the accuracy of the deterministic approach (15,23,24,29,38,48).

II. METHODS

II.1 Deterministic 3D mass-action / mean-field approach

Let us first describe the deterministic model of Ca^{2+}-dependent exocytosis. For the sake of simplicity, we consider the case of a single dominant Ca^{2+} buffer with a single Ca^{2+} ion binding site, as described by the reaction

$$B + Ca^{2+} \underset{k^-}{\overset{k^+}{\rightleftharpoons}} B^*. \tag{1}$$

Here B and B^* represents the free buffer and Ca^{2+}-bound buffer molecules, respectively (i.e. $B^*=CaB$), and k^+ (k^-) are the Ca^{2+}-buffer binding (unbinding) rates. Assuming isotropic diffusion and mass-action kinetics, this yields the following mass-action reaction-diffusion system (53-55):

$$\begin{cases} \dfrac{\partial Ca}{\partial t} = D_C \nabla^2 Ca - k^+ B \cdot Ca + k^- B^* + \sigma_{Ca}\delta(\mathbf{r}-\mathbf{r}_{Ca}) - \sigma_S(\mathbf{r},\mathbf{t}), \\ \dfrac{\partial B}{\partial t} = D_B \nabla^2 B - k^+ B \cdot Ca + k^- B^*, \\ \dfrac{\partial B^*}{\partial t} = D_B^* \nabla^2 B^* + k^+ B \cdot Ca - k^- B^*, \end{cases} \tag{2}$$

where D_B , D^*_B and D_C are the diffusivities of the free buffer, bound buffer and Ca^{2+}, respectively, and *Ca, B* and B^* denote concentrations of Ca^{2+}, free buffer and Ca^{2+}-bound buffer, respectively. The delta function indicates a point source (channel) centered at location $\mathbf{r_{Ca}}$, with amplitude $\sigma_{Ca} = I_{Ca}/(2F)$ where I_{Ca} is the Ca^{2+} current strength, and F is the Faraday constant. The sink term σ_S describes Ca^{2+} binding to the model exocytosis sensor, as will be explained further below (see Eqs. 6-7).

We take a simple cube as the diffusion domain, with zero flux boundary conditions for Ca^{2+} and buffer on all boundaries. Reflective boundary conditions are well suited for simulating an array of Ca^{2+} channels on a large section of a flat cell membrane. Further, reflective boundary conditions ensure non-negligible probability of Ca^{2+} binding to a model exocytosis Ca^{2+} sensor (see below) within a short time after the channel opening, even if only 20 Ca^{2+} ions enter the model volume during the 1ms-long current pulse (see Figs. 1-2). Replacing no-flux conditions with Robin boundary conditions simulating Ca^{2+} pumps and exchangers on the part of the boundary containing the channel would be more realistic, but would introduce the same type of bimolecular Ca^{2+}-binding reactions already present in this model, and therefore would not substantially impact the comparison of stochastic and deterministic simulation results.

The reaction-diffusion system given by Eqs. 2 is locally coupled to reactions describing a single stationary Ca^{2+} binding exocytosis sensor, with parameters inferred from the studies of neurotransmitter release at the calyx of Held synapse (56,57):

$$S_0 \underset{k^-}{\overset{5k^+Ca}{\rightleftharpoons}} S_1 \underset{2bk^-}{\overset{4k^+Ca}{\rightleftharpoons}} S_2 \underset{3b^2k^-}{\overset{3k^+Ca}{\rightleftharpoons}} S_3 \underset{4b^3k^-}{\overset{2k^+Ca}{\rightleftharpoons}} S_4 \underset{5b^4k^-}{\overset{k^+Ca}{\rightleftharpoons}} S_5 \overset{\gamma}{\rightarrow} \mathbf{R}. \tag{3}$$

The rate parameters are k^-=8.43 ms^{-1}; k^+=0.116 μM^{-1}ms^{-1}; b=0.25; γ=7.0 ms^{-1} (except Figure S1 of the Supporting Material, where the binding rate k^+ is increased by a factor of 10). This reaction is converted to a system of deterministic ODEs describing the Markovian transitions between distinct sensor states:

$$\begin{cases} \dfrac{d\langle S_0\rangle}{dt} = k^-\langle S_1\rangle - 5k^+\langle Ca\rangle_S\langle S_0\rangle, \\ \ldots \\ \dfrac{d\langle S_5\rangle}{dt} = -5b^4k^-\langle S_5\rangle + k^+\langle Ca\rangle_S\langle S_4\rangle - \gamma\langle S_5\rangle, \\ \dfrac{d\langle R\rangle}{dt} = \gamma\langle S_5\rangle. \end{cases} \tag{4}$$

Here $\langle \mathrm{Ca}\rangle_S$ is the time-dependent [Ca^{2+}] averaged over a small spherical volume describing the sensor, obtained by numerically solving Eq. 2, whereas $\langle S_{1..5}\rangle$ and $\langle R\rangle$ are the time-dependent occupancy probabilities of the distinct states of the single-copy sensor. In this simplified approach, all rates in Eq. 4 are deterministic, with the forward binding rates proportional to the time-dependent but deterministic local Ca^{2+} concentration, $\langle \mathrm{Ca}\rangle_S$. Thus, Eq. 4 represents a mean-field description, neglecting stochasticity in the binding rates caused by local Ca^{2+} fluctuations. Nevertheless, this deterministic mean-field approach allows to estimate the fluctuation in the FPT to the fully-bound state R by computing its probability density, given by the transition rate to this final absorbing state (58):

$$\frac{d\langle R\rangle}{dt} = \rho_{FPT}(t). \tag{5}$$

The primary goal of this study is to compare the FPT density (FPTD) given by Eq. 5 with the one obtained using fully stochastic simulation explained in the next subsection (see Figs. 1-3), in order to reveal the quantitative impact of various fluctuation sources on the latency to vesicle release.

In the simplest deterministic implementations of Ca^{2+} signaling models, the sink term in Eq. 2 is usually ignored, and therefore Ca^{2+} is not fully conserved. However, the binding of Ca^{2+} to exocytosis sensor can become significant when the Ca^{2+} influx current is small. As has been pointed out previously (24,29), failure to account for the binding-induced Ca^{2+} depletion is not an inherent deficiency of the deterministic approach, and can be corrected by restoring full Ca^{2+} conservation. In our implementation, this is achieved by adding a localized Ca^{2+} sink term in Eqs. 2:

$$\sigma_S(\mathbf{r},t) = g(\mathbf{r}-\mathbf{r}_S)q(t). \tag{6}$$

Here $g(\mathbf{r}-\mathbf{r}_S)$ has a finite support defined by the sensor volume, centered at the sensor location $\mathbf{r}_S$, with a total volume integral of 1, whereas $q(t)$ is the total Ca^{2+} flux induced by the sensor reactions in Eq. 4:

$$\begin{aligned} q(t) = {} & k^+\langle Ca\rangle_S\left(5\langle S_0\rangle + 4\langle S_1\rangle + 3\langle S_2\rangle + 2\langle S_3\rangle + \langle S_4\rangle\right) \\ & - k^-\left(\langle S_1\rangle + 2b\langle S_2\rangle + 3b^2\langle S_3\rangle + 4b^3\langle S_4\rangle + 5b^4\langle S_5\rangle\right). \end{aligned} \tag{7}$$

In our model, the sensor position $\mathbf{r}_S$ in Eq. 6 is close to the channel location $\mathbf{r}_{Ca}$, as shown in Fig. 1A,B. The distance between the two is either 33 nm (Figs. 1-3 and Fig. S2 of the Supporting Material) or 83 nm (Fig.

S1 of the Supporting Material). The deterministic simulation system is described by Eqs. 2-7, and satisfies exact Ca^{2+} conservation. However, in order to fully quantify the impact of this binding-induced Ca^{2+} depletion, we will repeat all simulations with and without the σ_S sink term in Eq. 2.

Note that Eqs. 2-7 describe the Ca^{2+} sensor as a *volume reactivity* (Doi) model, whereby the binding reaction takes place within a certain finite volume at a given time-dependent rate. In contrast, the same sensor binding is treated as a *surface reactivity* (Smoluchowski) model in the stochastic simulation described in the next subsection, whereby the reaction takes place with certainty when the Ca^{2+} ion is within the binding distance of the sensor (59,60). Nevertheless, the two sets of results are remarkably close to each other (see Figs. 1-2), with the sensor's binding radius (the support of $g(\mathbf{r})$ in Eq. 6) constituting one free matching parameter, set to roughly equal the Smoluchowski binding radius in the stochastic approach. We note that the exact Ca^{2+} conservation is exactly satisfied for any value of this parameter. In principle this extra parameter could be avoided by using the surface reactivity model in the deterministic approach as well, but at the expense of greater complexity of implementing the prescribed flux given by Eq. 7 as a time-dependent boundary condition on the sensor's surface.

Biologically, exocytosis sensors are positioned around the base of a vesicle, the latter acting as an obstacle to diffusion (13). However, we deliberately excluded vesicles and other obstacles from our comparative analysis, since they would not contribute to the discrepancy between deterministic and stochastic simulations arising from the neglect of local Ca^{2+} fluctuations, unless molecular crowding effects are taken into account. The effect of diffusion obstacles on exocytosis has already been explored in detail (13,46,61-66).

All deterministic reaction-diffusion simulations are performed using the CalC ("Calcium Calculator") software (67,68).

II.2 Stochastic approach

Stochastic approach allows a more realistic modeling of the biochemical pathways leading to vesicle release, taking into account relevant fluctuations, albeit at the computational expense of repeated trials of an appropriate Markov Chain Monte Carlo (MCMC) simulation. However, accurately combining diffusion with second-order bi-molecular reactions described by Eqs. 3 is an inherently complex issue for both the deterministic approach and the stochastic approach. Since this study aims to compare these two types of computation, it is important to recognize the different methods used to combine stochastic reaction and diffusion (6-9,44,59,69-71):

1) First Passage-Time Kinetic Monte-Carlo method (FPKMC) (72-74) directly combines stochastic bi-molecular binding with Brownian diffusion using an exact, event-based approach. This algorithm takes into account excluded volume and crowding effects. Approximate implementations include the Green's Function Reaction Dynamics method (GFRD) (75,76)) and the Cellular Dynamics Simulator (77). FPKMC has also been extended to the Doi volume reactivity model of bimolecular binding (60).

2) Discrete-time particle-based Brownian reaction dynamics (BRD) simulators (e.g. Smoldyn (78), MCell (79), GridCell (80)) can be viewed as approximations of the FPKMC/GFRD method. Since bi-molecular binding probability is not modeled exactly by a finite time-step method, convergence of results with time step size has to be carefully checked.

3) Course-grained stochastic simulation algorithm referred to as the Reaction-Diffusion Master Equation (RDME) method (e.g. SmartCell (81), MesoRD (82), URDME (83), STEPS (84), Lattice Microbes (85)) implement reactions *exactly* in elementary sub-volumes using the Gillespie stochastic simulation algorithm (86), assuming that reactants are well-mixed in each sub-volume. Diffusion is treated as an exchange reaction between neighboring voxels. Spatial resolution is limited by sub-volume size, which cannot be arbitrarily reduced without losing all reactions (59,60,87-89). A convergent modification of this approach resolves the latter problem by allowing reactions between neighboring cells (90).

A large variety of hybrid methods have also been developed, for instance methods combining the advantages of RDME and BRD algorithms (27,91,92), as well as hybrid methods combining in various ways the stochastic and deterministic reaction-diffusion components (14-16,30,93-98). Finally, for larger number of reactants, the Langevin approximation and formulations based on stochastic partial differential equations can be used (8,71,99-101).

For our comparative study, we will use Smoldyn (78), a particle-based BRD method, because of its flexibility, ease of use, and computational efficiency. This algorithm uses the Smoluchowski surface-reactivity model of bi-molecular reaction, with binding radii calibrated by approximate matching of the corresponding macroscopic mass-action reaction rates, making this method particularly well-suited for comparing with the deterministic mass-action simulation approach. This allows us to use the same reaction and diffusion parameters values in the stochastic and in the deterministic model of Ca^{2+} buffering and diffusion, without modification. It should be remembered however that the relationship between the macroscopic binding rates ("propensities") and the underlying microscopic binding radius is a separate, nontrivial problem (8,59,60,78,88,102-104). Moreover, the functional form of mass-action bimolecular reaction rate is known to be violated at large densities (105,106). However, it is precisely the sum of all sources of quantitative discrepancy between straightforward mass-action and stochastic approaches that we want to investigate in this study.

To check the convergence of results with respect to the time step size, we repeated Smoldyn simulations for a range of time steps. In the results shown in Figs. 1,2,S2, the time step size is set to Δt=1μs, while Δt=0.2μs was used for the case of larger Ca^{2+}-sensor binding rates in Fig. S1. Stochastic simulations corresponding to Figs. 1,2,S1,S2 took several weeks of computation time on two multi-core workstation with 24 simultaneous Smoldyn threads, while the corresponding deterministic simulations take less than one CPU-minute.

III. RESULTS

III.1 Spatially resolved 3D model

From a practical point of view, local fluctuations in Ca^{2+} concentration ultimately reveal themselves through the fluctuations in the latency to vesicle membrane fusion or other macroscopic Ca^{2+}-dependent effects, which is the most important observable in the modeling of Ca^{2+}-dependent exocytosis. Therefore, in our comparison of deterministic and stochastic modeling of vesicle release, we will focus on the latency between the opening of a Ca^{2+} channel, and the time of fusion of nearby vesicle(s). This latency is given by the first passage time (also known as the *waiting time* or *hitting time*) to the fully bound final "release" state R of the vesicle's putative Ca^{2+} sensor (13,14,46-51). We assume that the binding kinetics are described by Eqs. 3-5, inferred from the studies of the calyx of Held synapse (56,57). The qualitative

conclusions of this work however do not depend on the type of model used for the sensor. In our simulations of 3D Ca^{2+} diffusion, buffering and binding, illustrated in Fig. 1, the sensor is located at a distance of 33nm away from the channel, within the channel's "*nanodomain*". The sensor position is marked by a square in the bottom-left corner of the diffusion volume in Fig. 1A,B: the two panels illustrate one time frame of the deterministic and stochastic simulation, respectively, as described in Methods and the figure caption.

In the full stochastic approach, each MCMC trial provides one sample of the Markovian sensor state transition time series shown in Fig. 1D, driven in turn by the stochastic Brownian motion of Ca^{2+} and buffer particles illustrated in Fig. 1B. The simulation is repeated to construct a histogram estimate of FPTD. In Fig. 1E, the resulting FPTD estimate is shown as a black curve, and was obtained using about 10^8 Smoldyn iterations, each of which in turn comprises thousands of elementary MCMC iterations updating particle positions and binding states. In contrast, in the deterministic mean-field approach the FPTD is computed as the rate of change of the occupancy of the final absorbing state of the exocytosis sensor, obtained by numerically solving the coupled PDE-ODE reaction-diffusion problem (Eqs. 2-5). In Fig. 1E we directly compare FPTDs obtained using these two approaches, for the case when only N_{Ca}=100 ions enter the model volume during a 1ms-long Ca^{2+} channel current pulse. In this first comparison we set the binding sink term σ_S in Eq. 2 to zero, ignoring the depletion of Ca^{2+} ions due to their binding to the sensor. Figure 1E reveals a surprisingly good agreement between stochastic and deterministic simulations of FPTD, despite this simplification. Note that no curve scaling is involved, or would be appropriate, in comparing the FPTD obtained using the two methods. In fact, the total integral of FPTD is conserved and equals one: given a closed domain with reflective boundary conditions, full sensor binding eventually happens, with certainty. In instances when the stochastic FPTD appears smaller in amplitude compared to the deterministically computed FPTD (see Fig. 2B-D), the former must eventually become bigger than the latter later in the simulation. However, for the case of open boundary conditions and zero resting [Ca^{2+}], the integral of FPTD would represent total probability of release, which would be smaller than one.

Note that the peak of FPTD occurs soon after the end of the pulse because the Ca^{2+} sensor is close to the channel location, and because the pulse is sufficiently short so that the sensor is far from saturation during the pulse. However, Figure S1A of the Supporting Material shows that the peak of FPTD can occur before the end of the pulse for larger values of the sensor's Ca^{2+} binding rate.

Part of the discrepancy between the two methods seen in Fig. 1E is explained by the depletion of five Ca^{2+} ions as they bind to the Ca^{2+} sensor, which is absent from a straightforward implementation of the mass-action approach that doesn't include the feedback from the Ca^{2+}-sensor binding onto the local Ca^{2+} concentration (24,29). To reveal the effect of this Ca^{2+} ion depletion, in Fig. 2 we repeat the numerical solution of Eqs. 2-5 with and without the Ca^{2+} sink term, given by Eqs. 6-7. Simulations are then repeated for several values of Ca^{2+} current strength corresponding to different number of total Ca^{2+} ions entering the volume during a 1ms-long channel opening, from N_{Ca}=200 (Fig. 2A) down to N_{Ca}=20 (Fig. 2D). Note that the depletion correction almost fully abolishes the discrepancy between stochastic and deterministic simulations for the case of 100 Ca^{2+} ions, but not for smaller number of ions. These results suggest that deterministic results become unreliable when only ~40 or less Ca^{2+} ions enter the simulation volume (Figs. 2B-D).

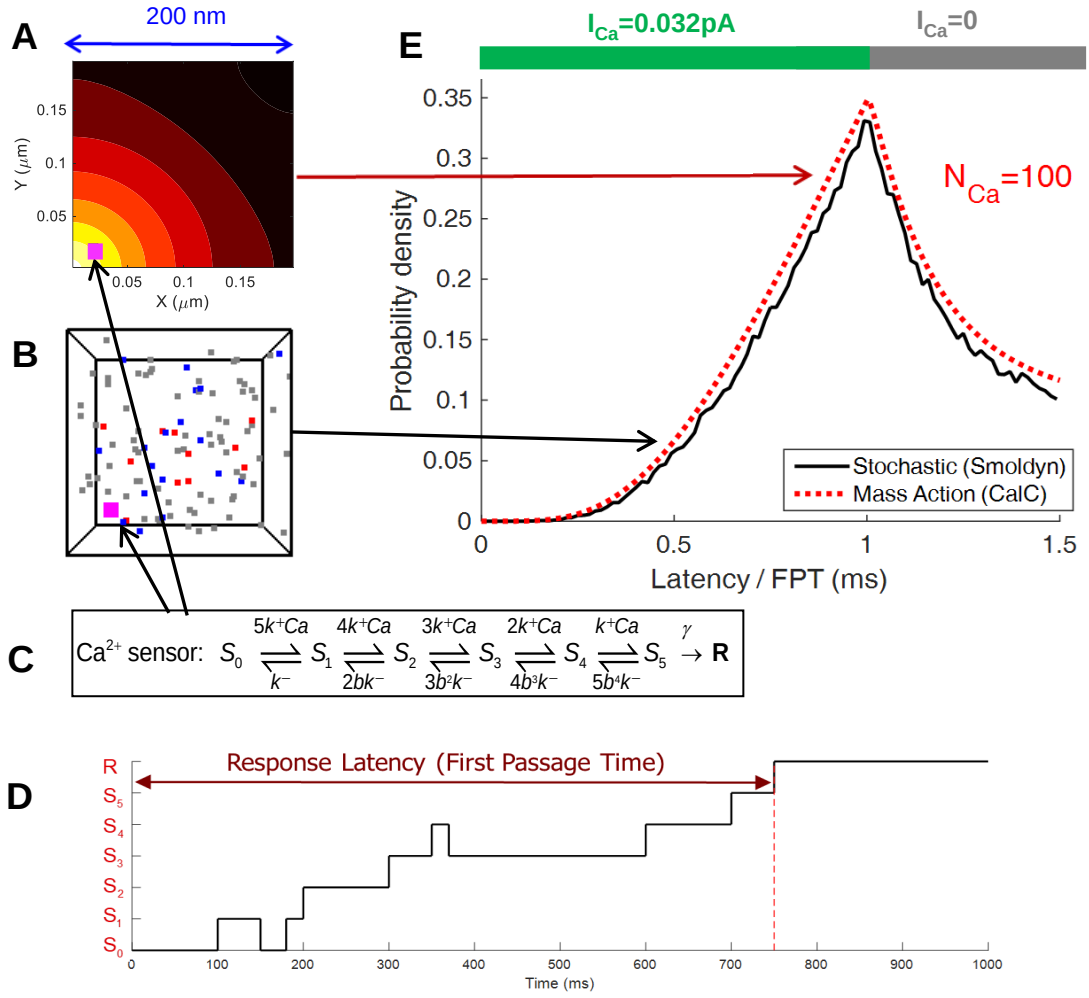

Figure 1. Deterministic vs. stochastic simulation of buffered Ca^{2+} diffusion and binding to a stationary sensor. Ca^{2+} and buffer molecules diffuse within a $(0.2\mu m)^3$ cube, with diffusivities D_{Ca}=0.2μm²/ms and D_B=0.05μm²/ms, respectively. Ca^{2+} sensor is 33nm away from a point Ca^{2+} source (Ca^{2+} channel) in the corner of the cube. Ca^{2+} current pulse of 0.032 pA lasts 1ms, letting in a total of 100 Ca^{2+} ions. Buffer has a concentration of 20μM and affinity of 1μM, corresponding to a total of 96 ions. **(A)** One time frame of a 2D slice of the mass-action simulation of $[Ca^{2+}]$ on a color-coded logarithmic scale, 0.2ms after Ca^{2+} channel opening. **(B)** One time frame of the stochastic Smoldyn iteration shows the locations of all tracked particles 0.2ms after Ca^{2+} channel opening (*magenta square*: Ca^{2+} sensor; *red squares*: Ca^{2+} ions; *gray and blue squares*: free and bound buffer molecules, respectively). Symbol sizes are not to scale. (**C**) Stationary vesicle fusion sensor undergoes 5 Ca^{2+} binding steps with progressively decreasing unbinding rate, i.e. increasing binding cooperativity (Eq. 4) (56,57), (**D**) Sensor state transition sequence illustrates a single MCMC trial of the stochastic Smoldyn simulation. FPT is computed from the start of the Ca^{2+} current pulse to the time of sensor transition to the final state ***R***. (**E**) Comparison of FPTD obtained from the histogram of stochastic trials shown in **D** (*black curve*), or from deterministic reaction-diffusion simulation (Eqs. 2-5) (*red dotted curve*), with binding depletion ignored (σ_S=0 in Eq. 2).

While full parameter sensitivity analysis is prohibitive in view of the computational cost of the full stochastic approach, we repeated the comparison of deterministic and stochastic simulations for two more combination of parameters, with results shown in Supporting Material. Namely, Figure S1 repeats this

comparison after the sensors' Ca^{2+} binding rate is increased by a factor of 10, corresponding to an unrealistically large sensor binding radius. To compensate for such a large Ca^{2+} binding rate, we also increased the distance from the Ca^{2+} channel to the release sensor, from 33nm to 83nm. As Fig. S1 shows, in this case the depletion correction (Eqs. 6-7) is critical for achieving good agreement between the two approaches even for a relatively large number of Ca^{2+} ions, and peak FPTD occurs before the end of the pulse, due to faster saturation of the Ca^{2+} sensor caused by the larger binding rate. Finally, in Figure S2 we compare stochastic and deterministic simulations for the same parameters as in Fig. 2, but for the case of a Ca^{2+} sensor that only binds two Ca^{2+} ions. Despite significant difference in parameters used in Figs. 2, S1 and S2, in particular very different release probability and FPTD profile, in all three cases the discrepancy between stochastic and depletion-corrected mean-field simulations becomes apparent only when the total number of entering Ca^{2+} ions falls below about 40-50.

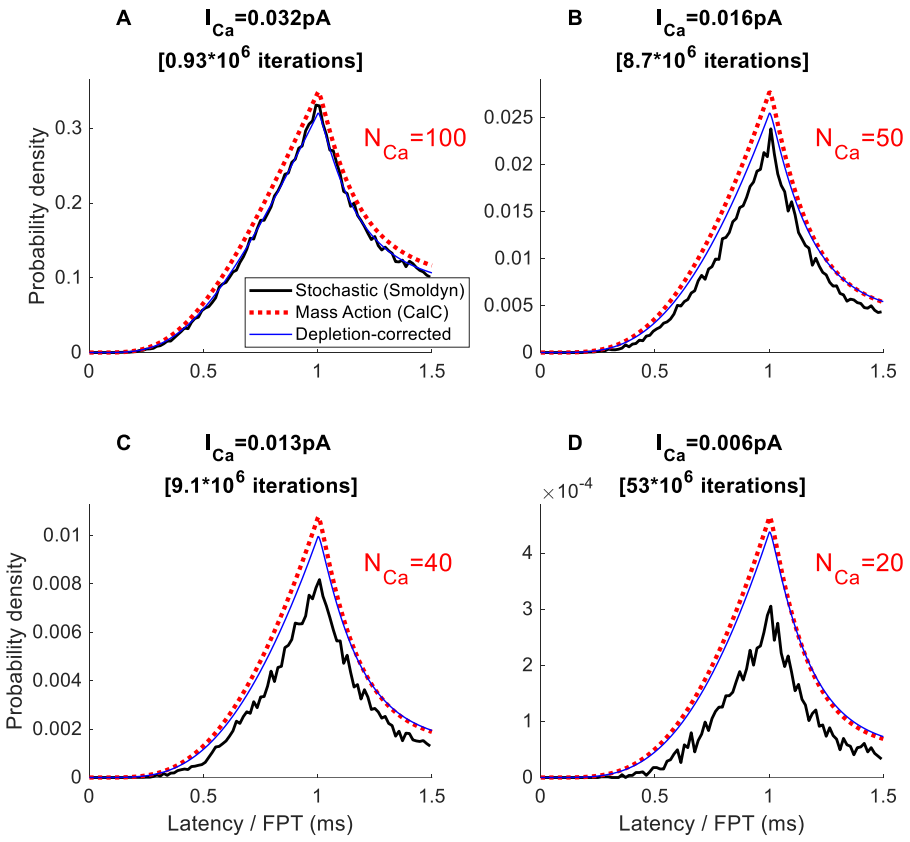

Figure 2. Mass-action vs stochastic estimation of FPTD in response to a 1ms-long Ca^{2+} current pulse of varying amplitudes. All parameters as in Fig. 1, except for the varying Ca^{2+} current values and the total number of Ca^{2+} ions entering during the 1-ms current pulse (N_{Ca}), as indicated in text labels. In all panels, *black solid curves* represent the histograms of FPT to full sensor binding, the *dotted red* curves show the corresponding deterministic estimate of FPTD (Eq. 5), with binding depletion ignored (σ_S=0 in Eq. 2), while the *solid blue* curves show the deterministic estimate of FPTD, with binding depletion taken into account (Eqs. 6-7). Note the great difference in scale: the cumulative probability of full binding within 1.5 ms of channel opening is about 18% in *A* (N_{Ca}=100), while in *D* (N_{Ca}=20) it is on the order of 10^{-4}, explaining the large number of MCMC trials required in the latter case, since most binding events happen in the long tail of this distribution.

Figs. 2B-D show that the stochastically computed FPTD is smaller in amplitude compared to the one computed using mean-field methods during and shortly after the Ca^{2+} current pulse, which indicates that the deterministic approach overestimates true release probability over physiological time scales. However, as mentioned above, this relationship between the FPTD curves obtained using the two approaches is bound to invert later after the pulse, since the cumulative probability of full binding equals one.

The close agreement between the two approaches for such small total numbers of Ca^{2+} ions is *a priori* surprising. As will be explained more fully below, the reason is the small size of the correlation between the local number of Ca^{2+} ions in the vicinity of the exocytosis sensor on the one hand, and the Ca^{2+}-binding state of the sensor on the other hand. Figure 3 compares the size of this correlation for the same parameter values as in Fig. 2A,B,D, when to the total number of Ca^{2+} ions entering during the 1ms-long pulse is either N_{Ca}=20, 50, or 100. Figure 3A shows the average number of Ca^{2+} ions within a small $(20nm)^3$ box surrounding the exocytotic sensor, n_{Ca}, measured shortly (t=0.1ms) after the channel closing, measured when the sensor is in one of 6 states (see Eq. 3), S_0 through S_5. This conditional average of n_{Ca}, $\langle n_{Ca} \mid S_k \rangle$, is compared to the unconditional average of n_{Ca} at the same time point, shown as dashed curves. The ratio between the conditional and unconditional average values of n_{Ca} is an appropriate measure of correlation between n_{Ca} and S_k, and is shown in in Fig. 3B. Note that this ratio deviates from 1 by no more than 10% when N_{Ca}=100, explaining the good agreement between stochastic and deterministic simulations in this case. In contrast, $\langle n_{Ca} \mid S_4 \rangle$ and $\langle n_{Ca} \mid S_5 \rangle$ are up to 50% smaller than $\langle n_{Ca} \rangle$ when N_{Ca}=20, violating the crucial assumption of the deterministic mean-field approach that n_{Ca} and the sensor state are independent quantities.

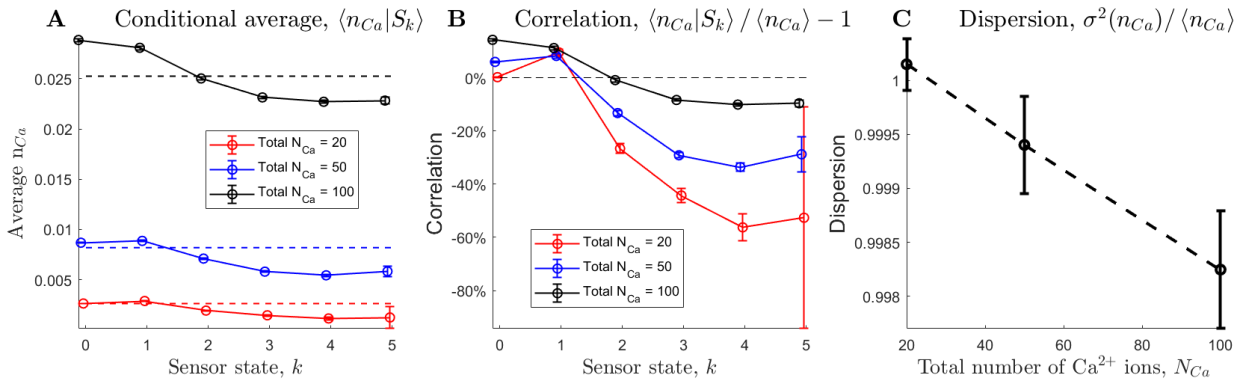

Figure 3. Correlation between the state of the Ca^{2+} sensor, S_k, and the number of Ca^{2+} ions, n_{Ca}, in a box of size $(20nm)^3$ surrounding the sensor. All parameter values are the same as in Fig. 2A,B,D**. (A)** Average n_{Ca} at t=0.1ms after channel closing, conditional on the sensor state S_0 through S_5. The corresponding unconditional average values of n_{Ca} at the same time point, $\langle n_{Ca} \rangle$, are shown as dashed lines. **(B)** The ratio of the conditional and unconditional average of n_{Ca} as a measure of correlation between n_{Ca} and the sensor state. The absolute size of the correlation reaches 50% for N_{Ca}=20 (red curve), while it is no greater than 10% for N_{Ca}=100 (black curve). Error bars indicate statistical uncertainty obtained by standard bootstrap resampling of the simulated data set. **(C)** Statistical properties of n_{Ca} quantified by the dispersion (variance-to-mean ratio) remains very close to 1 for all three values of N_{Ca}, indicating Poisson statistics.

To see even more clearly the connection between the correlation size and the discrepancy between stochastic vs. mean-field results, we will now turn to a simplified compartment-based model of this reaction-diffusion process.

III.2 Analysis of a simplified two-compartment model

To gain an intuitive understanding of the factors affecting the relative accuracy of the deterministic mean-field approach, we will analyze a highly simplified model of Ca^{2+} diffusion and binding shown in Fig. 4, similar to the one analyzed by S.H. Weinberg (48) (see also (26,52)). This reduced model consists of two well-mixed compartments of Ca^{2+} ions, with the Ca^{2+} sensor for exocytosis contained within the inner compartment. We assume that the sensor can bind two Ca^{2+} ions before triggering exocytosis, according to the reaction

$$S_0 \underset{k_1^-}{\overset{k_1^+ n}{\rightleftharpoons}} S_1 \underset{k_2^-}{\overset{k_2^+ n}{\rightleftharpoons}} S_2 \overset{\gamma}{\rightarrow} \mathbf{R}, \tag{8}$$

where n is the number of free Ca^{2+} ions in the sensor sub-compartment. For the sake of simplicity, the stoichiometric factors of 2 are absorbed into the definitions of the forward and backward binding rates, $k_{1,2}^{\pm}$ We set $k_1^+ = 2$, $k_1^- = 1$, $k_2^+ = 1$, $k_2^- = 2$, $\gamma = 2$.

Diffusion is represented as transitions between the two compartments, with forward and backward transitions rates equal to α and β, respectively:

$$n_{Bulk} \underset{\alpha}{\overset{\beta}{\rightleftharpoons}} n, \tag{9}$$

where the n_{Bulk} is the number of free Ca^{2+} ions in the bulk compartment, given by

$$n_{Bulk} = N - n - n_{Bnd}. \tag{10}$$

Here N=const is the total number of Ca^{2+} ions in both compartments, and n_{Bnd} is the number of sensor-bound Ca^{2+} ions, determined by the occupancies of all Ca^{2+}-bound sensor states, indicated by angled brackets (for precise notation description, see Appendix, Eq. 16):

$$n_{Bnd} = \langle S_1 \rangle + 2\langle S_2 \rangle + 2\langle R \rangle \leq 2 \tag{11}$$

The ratio of diffusion rates α and β in Eq. 9 implicitly defines the ratio of the volumes of the two compartments. The total number of Ca^{2+} ions, N, is a constant parameter: initial condition is set by adding N ions to the bulk compartment. Therefore, initially there are no ions in the sensor compartment, nor bound to the sensor: $n(0)=n_{\mathrm{Bnd}}(0)=0$ (alternative initial conditions were also explored, but did not provide significant new insights). Even though Ca^{2+} buffering is not explicitly implemented in this simplified model, buffering can be viewed as being part of the exchange reaction with the bulk compartment described by Eq. 9, whereby buffer-bound Ca^{2+} ions are to be understood as belonging to the bulk (non-sensor) compartment.

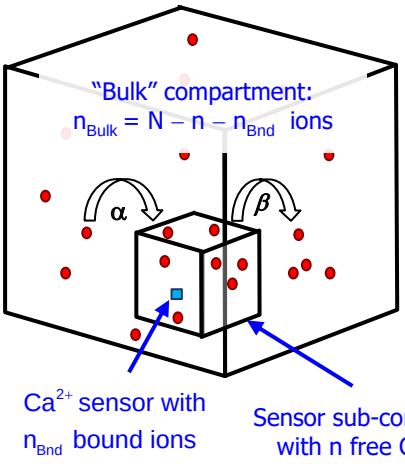

Figure 4. Two-compartment model of Ca^{2+} diffusion and sensor binding. The inner compartment contains n ions of Ca^{2+}, which can bind to the Ca^{2+} sensor. The inner compartment exchanges ions with the bulk compartment with diffusive rates α and β. The total number of ions equals N and is conserved, therefore there are $n_{Bulk}=N-n-n_{Bnd}$ ions in the bulk compartments, where n_{Bnd} is the number of ions bound to the sensor, as described by Eq. 11. At initial time, all N particles are added to the bulk compartment.

The stochastic implementation of this model is given by the following continuous-time Markov chain, with (n, S_k) and (n, R) denoting a state with n Ca^{2+} ions in the sensor sub-compartment, and the sensor in state S_k or in the final fusion state R:

$$
\begin{array}{ccccccccc}
(0,S_0) & \underset{\beta}{\overset{\alpha N}{\rightleftharpoons}} & (1,S_0) & \underset{2\beta}{\overset{\alpha(N-1)}{\rightleftharpoons}} & (2,S_0) & \underset{3\beta}{\overset{\alpha(N-2)}{\rightleftharpoons}} & (3,S_0) & \underset{4\beta}{\overset{\alpha(N-3)}{\rightleftharpoons}} \cdots \underset{N\beta}{\overset{\alpha}{\rightleftharpoons}} & (N,S_0) \\
 & & k_1^+ \downarrow\uparrow k_1^- & & 2k_1^+ \downarrow\uparrow k_1^- & & 3k_1^+ \downarrow\uparrow k_1^- & & Nk_1^+ \downarrow\uparrow k_1^- \\
(0,S_1) & \underset{\beta}{\overset{\alpha(N-1)}{\rightleftharpoons}} & (1,S_1) & \underset{2\beta}{\overset{\alpha(N-2)}{\rightleftharpoons}} & (2,S_1) & \underset{3\beta}{\overset{\alpha(N-3)}{\rightleftharpoons}} & \cdots \underset{(N-1)\beta}{\overset{\alpha}{\rightleftharpoons}} & (N-1,S_1) \\
 & & k_2^+ \downarrow\uparrow k_2^- & & 2k_2^+ \downarrow\uparrow k_2^- & & & (N-1)k_2^+ \downarrow\uparrow k_2^- \\
 & & (0,S_2) & \underset{\beta}{\overset{\alpha(N-2)}{\rightleftharpoons}} & (1,S_2) & \underset{2\beta}{\overset{\alpha(N-3)}{\rightleftharpoons}} & \cdots \underset{(N-2)\beta}{\overset{\alpha}{\rightleftharpoons}} & (N-2,S_2) \\
 & & \downarrow\gamma & & \downarrow\gamma & & & \downarrow\gamma \\
 & & (0,R) & \underset{\beta}{\overset{\alpha(N-2)}{\rightleftharpoons}} & (1,R) & \underset{2\beta}{\overset{\alpha(N-3)}{\rightleftharpoons}} & \cdots \underset{(N-2)\beta}{\overset{\alpha}{\rightleftharpoons}} & (N-2,R)
\end{array}
\tag{12}
$$

This model is almost equivalent to the one analyzed by S.H. Weinberg (48) (see Eq. 2.8 therein), except that we compare this model with a similar two-compartment deterministic representation of the same process, rather than its single-compartment reduction, allowing us to clearly separate the effects of binding-induced Ca^{2+} ion depletion from the impact of stochastic fluctuations. Another difference of our approach is that we consider the bulk compartment of a finite volume. Therefore, no particle number truncation is required, since the total number of Ca^{2+} ions is conserved and set equal to N.

The Markov Chain described by Eqs. 12 is readily converted to linear Chemical Master Equations (CME) describing the evolution of state probabilities, d**p**/dt = W**p**, where vector **p** has $4N-1$ states shown in Eq. 12 . We note parenthetically that the number of states can be further reduced using sensor state conservation law and by collapsing together all (n, R) states. The CME system is shown explicitly in Eq. 15 of the Appendix. The CME system can in turn be converted (using appropriate summations) to the ODEs for the moments of the state variables, i.e. the occupancy probabilities of sensor states $\langle S_k \rangle$ and $\langle R \rangle$, and the

moments of the Ca^{2+} ion number n conditional on the state of the sensor, denoted as $\langle n^m | S_k \rangle$ (see Appendix). The first five of these moment equations read:

$$\begin{aligned}
\frac{d\langle S_0\rangle}{dt} &= k_1^-\langle S_1\rangle - k_1^+\langle n\,|\,S_0\rangle\langle S_0\rangle,\\
\frac{d\langle S_1\rangle}{dt} &= k_2^-\langle S_2\rangle - k_2^+\langle n\,|\,S_1\rangle\langle S_1\rangle - k_1^-\langle S_1\rangle + k_1^+\langle n\,|\,S_0\rangle\langle S_0\rangle,\\
\frac{d\langle S_2\rangle}{dt} &= -k_2^-\langle S_2\rangle + k_2^+\langle n\,|\,S_1\rangle\langle S_1\rangle - \gamma\langle S_2\rangle,\\
\frac{d\langle R\rangle}{dt} &= \gamma\langle S_2\rangle = \rho_{FPT}(t),\\
\frac{d\langle n\rangle}{dt} &= -k_1^+\langle n\,|\,S_0\rangle\langle S_0\rangle - k_2^+\langle n\,|\,S_1\rangle\langle S_1\rangle + k_1^-\langle S_1\rangle + k_2^-\langle S_2\rangle + \alpha\left(N - n_{\mathrm{Bnd}} - \langle n\rangle\right) - \beta\langle n\rangle.
\end{aligned} \tag{13}$$

Here n_{Bnd} is given by Eq. 11 and denotes the total number of Ca^{2+} ions bound to the sensor, while ρ_{FPT} denotes the FPTD. The evolution equations for the first moments $\langle n \mid S_k \rangle$ are not shown, but are easily derived from the CME system; they depend in a somewhat complex way on higher moments $\langle n^2 \mid S_k \rangle$. Since we consider a finite number of Ca^{2+} ions, the system of moments is closed and always solvable in closed form due to the linearity of the CME system.

If the number of Ca^{2+} ions in the sensor compartment is independent of the sensor state, $\langle n|S_k\rangle = \langle n\rangle$, then Eq. 13 reduces to the deterministic, mean-field description of the same process,

$$\begin{aligned}
\frac{d\langle S_0\rangle}{dt} &= k_1^-\langle S_1\rangle - k_1^+\langle n\rangle\langle S_0\rangle,\\
\frac{d\langle S_1\rangle}{dt} &= k_2^-\langle S_2\rangle - k_2^+\langle n\rangle\langle S_1\rangle - k_1^-\langle S_1\rangle + k_1^+\langle n\rangle\langle S_0\rangle,\\
\frac{d\langle S_2\rangle}{dt} &= -k_2^-\langle S_2\rangle + k_2^+\langle n\rangle\langle S_1\rangle - \gamma\langle S_2\rangle,\\
\frac{d\langle R\rangle}{dt} &= \gamma\langle S_2\rangle = \rho_{FPT}(t),\\
\frac{d\langle n\rangle}{dt} &= -\langle n\rangle\left(k_1^+\langle S_0\rangle + k_2^+\langle S_1\rangle\right) + k_1^-\langle S_1\rangle + k_2^-\langle S_2\rangle + \alpha\left(N - \langle n_{\mathrm{Bnd}}\rangle - \langle n\rangle\right) - \beta\langle n\rangle.
\end{aligned} \tag{14}$$

Thus, this mean-field description is the simplest moment-closure of the stochastic description given by Eqs. 13 under the assumption of zero correlation between the state of the sensor and the number of ions in the sensor compartment. Therefore, the high variance in the local number of Ca^{2+} ions only indirectly affects FPTD, as long as the number of ions in the sensor sub-compartment is weakly correlated with the binding state of the release sensor.

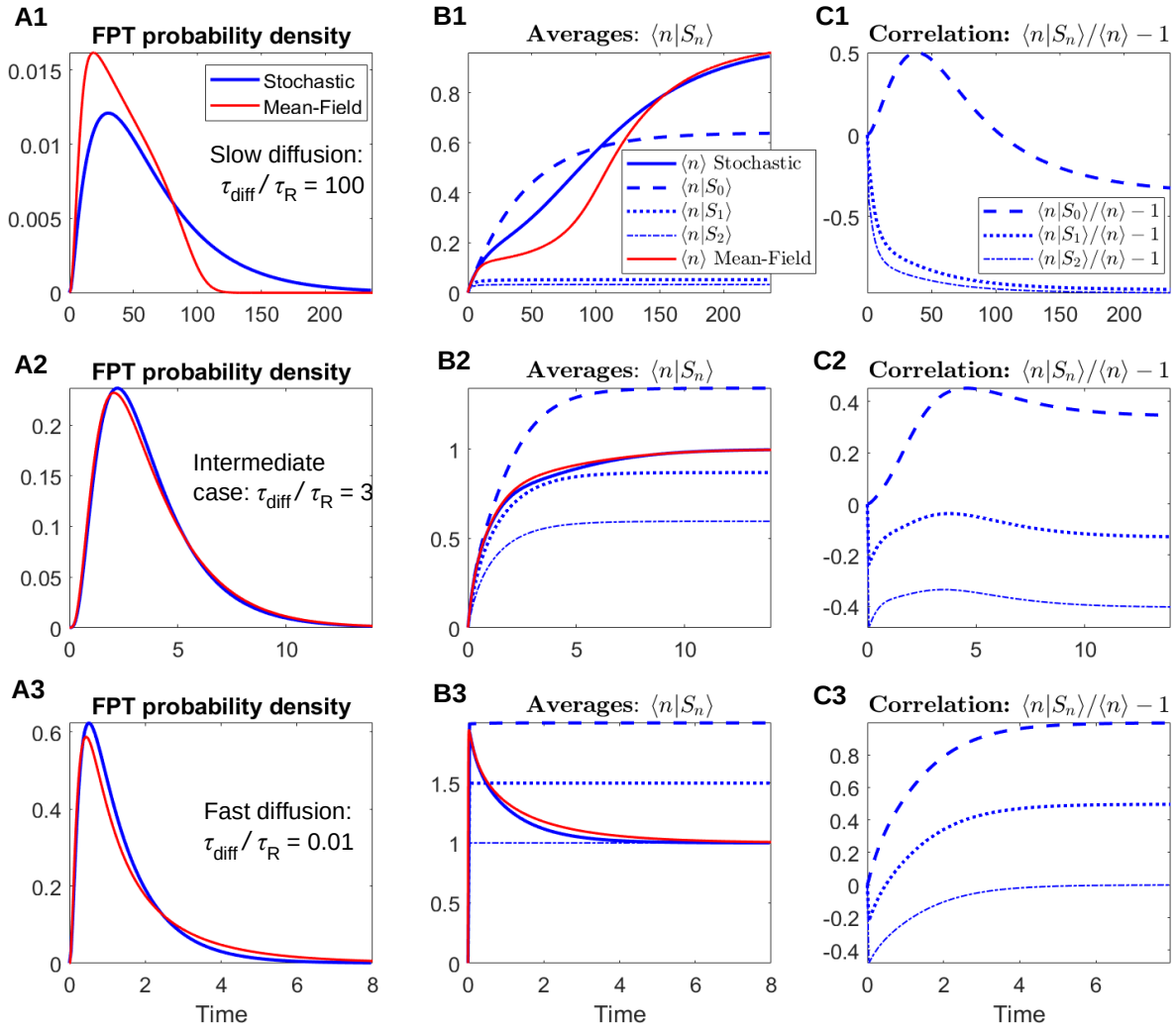

Figure 5. Comparison between mass-action and stochastic simulation of the two-compartment model in Fig. 4, for different ratios between diffusion and reaction time scales: τ_{diff}/τ_R=100 (**A1-C1**), τ_{diff}/τ_R=3 (**A2-C2**), and τ_{diff}/τ_R=0.01 (**A3-C3**). This ratio is controlled by varying the diffusion rate α=β=1/τ_{diff}, while keeping reaction rates constant. (**A1**,**A2,A3**) First-passage time to full binding probability density (FPTD). (**B1**,**B2,B3**) Average number of Ca^{2+} ions in the sensor compartment. For the stochastic simulation, also shown are the average number of Ca^{2+} ions conditional on the sensor state, $\langle n_{Ca}|S_k\rangle$. Note that the number of ions in the sensor compartment approaches n=1 in all cases, since the total number of Ca^{2+} ions is N=4. (**C1**,**C2,C3**) Correlation between the number of Ca^{2+} ions in the sensor compartment and the sensor state, given by the ratio of conditional and unconditional expectations $\langle n_{Ca}|S_k\rangle/\langle n_{Ca}\rangle$ (k=0,1,2).

This intuition is confirmed by the results shown in Fig. 5, where we compare the exact solution of the stochastic two-compartment model described by Eqs. 12-13 with the solution of the mean-field description given by Eq. 14. To reveal fully the impact of stochastic fluctuations, we will focus on the case where the number of Ca^{2+} ions is very small, and stochastic effects are expected to be most pronounced, namely N=4. The diffusion rates α and β are set to equal each other, to ensure that exactly one Ca^{2+} ion remains free (on average) inside the sensor sub-compartment upon equilibration, after 2 out of the 4 available Ca^{2+} ions

are bound by the sensor. Figure 5 shows this comparison between stochastic and mean-field results for three distinct ratios between diffusion and reaction rates: τ_{diff}/τ_R=100 (Fig. 5A1-C1), τ_{diff}/τ_R = 3 (Fig. 5A2-C2) and τ_{diff}/τ_R =0.01 (Fig. 5A3-C3). This ratio is controlled by varying the diffusion rate $\alpha = \beta = 1/\tau_{diff}$, while keeping the reaction rates constant ($\tau_R = 1/k_1^- = 1/k_2^+ = 1$). As Figure 5 demonstrates, the difference between the FPTD distributions obtained using the mean-field and stochastic approaches can be surprisingly small even for N=4~O(1). In agreement with the arguments above, the discrepancy between the FPTD obtained using the two approaches is the smallest for the case when the absolute correlation between the sensor state and the number of Ca^{2+} ions in the sensor sub-compartment shown in Fig. 5C1,C2,C3 is also the smallest, which happens for $\tau_{diff}/\tau_R \approx 3$. In this case diffusive fluctuations are sufficiently fast to partially "smooth out" the correlations between the sensor state and the number of Ca^{2+} ions in the sensor compartment. As in our 3D simulations (Fig. 3B), in Fig. 5C1-C3 the correlations are quantified in terms of the ratio of conditional and unconditional expectations of the Ca^{2+} ion number inside the sensor compartment, which are shown in Fig. 5B1,B2,B3.

The dependence of correlations on the τ_{diff}/τ_R ratio can be quite non-trivial, but intuitive. For example, in the case of slow diffusion (Fig. 5C1), $\langle n|S_{1,2}\rangle \ll \langle n\rangle$, so the corresponding correlation is negative and close to -1. In this case there is only a small probability of any ions remaining in the sensor compartment when at least one ion is bound to the sensor: the fact that the sensor is still not fully bound indicates that the remaining ions are most likely outside of the sensor compartment. In contrast, for fast diffusion (Fig. 5C3), the largest correlation approaches $\langle n|S_0\rangle / \langle n\rangle - 1 \to 1$, or $\langle n|S_0\rangle \approx 2\langle n\rangle$: when the sensor is unbound, there are on average n=N/2=2 Ca^{2+} ions inside the sensor compartment, which is twice as many as there will remain upon full sensor binding. Recall that we set $\alpha = \beta$, so ions quickly equipartition between the sensor compartment and the bulk in the limit of fast diffusion.

Interestingly, results shown in Fig. 5C1,C2,C3 suggest that the dependence of the maximal correlation size on the diffusive time scale is non-monotonic. This is confirmed by a more detailed comparison shown in Figure 6 as a function of the diffusive time scale, τ_{diff}=1/β (assuming again a constant reaction rate and $\alpha = \beta$, for the sake of simplicity).

Intuition suggests that in the limit $\tau_{diff} \to \infty$, diffusion is very slow on the time scale of the reaction, and therefore the correlation between the sensor state and the number of Ca^{2+} ions in the sensor compartment imposed by the Ca^{2+}-binding reaction is strong, resulting in a large error of the mean-field reduction of the problem. Figure 6 confirms this intuition, showing the growth of the discrepancy between stochastic and deterministic computation of FPTD as the diffusion rate decreases. However, Fig. 6C1,C2 also reveals that the dependence of FPTD discrepancy on diffusive time scale is non-trivial, reaching a minimum for certain fixed relationship between the rates of diffusion and reaction. Therefore, correlations between the sensor state and the number of Ca^{2+} ions in the sensor sub-compartment do not disappear as $\tau_{diff} \to 0$. In this limit, the numbers of Ca^{2+} ions in the bulk compartment and the sensor sub-compartment are in instantaneous equilibrium with each other, so a Ca^{2+} binding reaction leads to an immediate reduction of the latter. Thus, in the case of very fast diffusion, Ca^{2+}-binding reactions create strong negative correlations between the sensor state and the number of Ca^{2+} ions, which is lower in absolute magnitude than in the case of very slow diffusion, but still significant. Therefore, in the compartmental model, the discrepancy between mean-field and stochastic computations of FPTD achieve minimum for certain intermediate value of the ratio between the diffusion and reaction time scales. However, for larger number of Ca^{2+} ions, N_{Ca}=20, this non-monotonic relationship is less pronounced, as shown in Fig. 6A2,B2,C2.

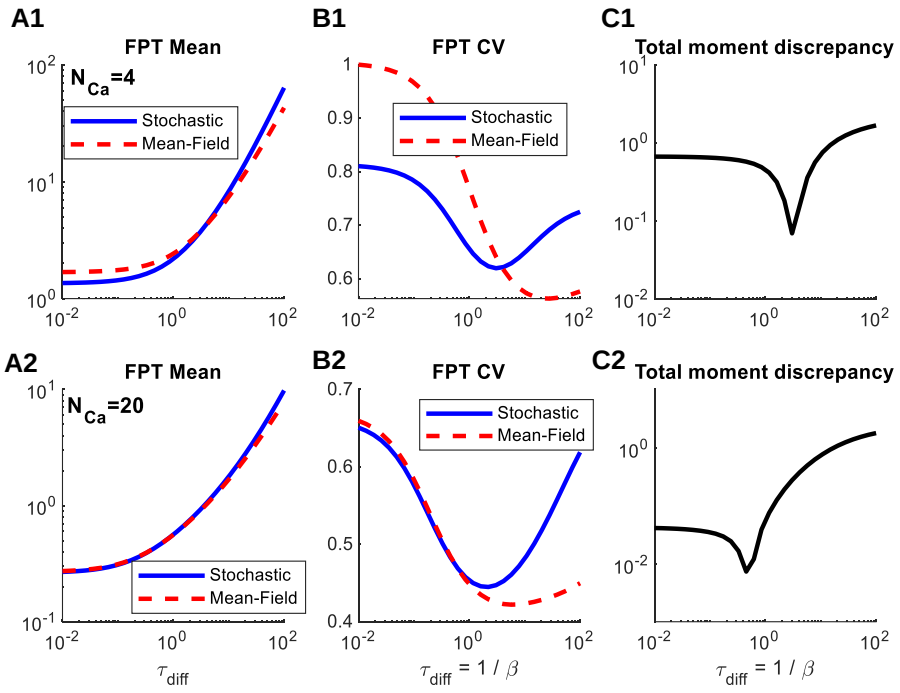

Figure 6. Comparison of the central moments of FPTD obtained using deterministic mean-field vs stochastic approaches, as a function of diffusive time constant $\tau_{diff}=1/\beta$, for two values of total particle number, *N*=4 (A1-C1) and *N*=20 (A2-C2). (**A**1, **A2**): FPT average, (**B1**, **B2**): coefficient of variance of FPT, (**C1**, **C2**): total normalized discrepancy of first 3 central moments of FPTD between stochastic and deterministic simulations. Diffusive rates satisfy $\alpha/\beta=1$ for all simulation conditions, ensuring that the average number of ions in the sensor compartment upon full sensor binding is *n*=1 in (A1-C1) and *n*=9 in (A2-C2).

Another way to understand the growing inaccuracy of the mean-field approach as $\tau_{diff}\to 0$ is that the two-compartment mean-field description given by Eq. 14 does not approach the physically correct model in this limit, since it does not take into account the immediate reduction of the free Ca^{2+} ion number *n* upon binding. In other words, in the limit $\tau_{diff}\to 0$ ($\alpha\to\infty, \beta\to\infty$), the number of ions in the sensor compartment is no longer an independent variable, and is directly determined by the sensor's binding state: $n\to\alpha(N-n_{Bnd})/(\alpha+\beta)$. Unlike the mean-field description, the stochastic description given by Eq. 13 remains meaningful for any values of rate parameters.

To show that these conclusions about the accuracy of mean-field approach in the compartmental model do not depend on the details of the Ca^{2+} binding reaction, in Figures S3 and S4 of Supporting Material we repeat our analysis for the case of a Ca^{2+} sensor with five cooperative binding sites, which we also used in our 3D simulations (Eq. 3). Figs. S3,S4 show that the general trends illustrated in Figs. 5,6 also hold for this more complex sensor model.

IV. Discussion

Our main finding is that the discrepancy between stochastic and deterministic simulation of Ca^{2+} diffusion and bi-molecular binding/unbinding reactions can in certain cases be much smaller than expected from naïve intuition (i.e., naïve application of $1/\sqrt{N_{Ca}}$ scaling). This result has very practical significance, since stochastic Ca^{2+} channel gating (and more generally, fluctuating Ca^{2+} current) is computationally inexpensive to simulate and combine with deterministic mass-action reaction-diffusion equations, providing an efficient hybrid method for the modeling of Ca^{2+}-dependent phenomena (7,14,30).

However, we want to emphasize once again that the accuracy of such an approach was shown to be greatly reduced in the presence of positive feedback on Ca^{2+} influx provided by CICR (19-28,107). We should point out that recent studies suggest that CICR does contribute to both pre- and post-synaptic processes (108-112). Still, it is useful and important to explore the impact of fluctuations on each part of the biochemical pathways to vesicle release, including those not involving CICR.

To complement prior work on the role of stochastic fluctuations in Ca^{2+}-dependent mechanisms, we considered a maximally reduced model to focus on two sources of stochasticity downstream of Ca^{2+} influx, namely the diffusive fluctuations in Ca^{2+} concentration, and the fluctuations due to Ca^{2+} binding and unbinding reactions. Further, following several prior studies (13,14,46-51), we focused on the modeling of FPTD, which can be considered as the true "output observable" whose uncertainty combines all upstream sources of stochasticity in this biochemical process. Considering such maximally simplified, reduced model allowed us to study more directly the interplay between fluctuations due to diffusion and reaction in determining the final fluctuations in the Ca^{2+} sensor binding time.

Simulations of the reduced spatially-resolved model revealed that the distribution of FPT to full binding of the exocytotic Ca^{2+} sensor is accurately predicted by the mass-action / mean-field approach, as long as the number of Ca^{2+} ions is above about 50. This rough estimate of the threshold of accuracy seems to be relatively stable with respect to several parameters of the model, as seen by comparing Figs. 2, S1 and S2, which differ considerably in several critical model parameters. We note that this is a surprising result, given the presence of multiple bimolecular reactions, since the associated nonlinearities are expected to amplify the impact of fluctuations in the local Ca^{2+} ion concentration (44). Intuition may suggest that buffering "washes out" stochastic fluctuations in the local Ca^{2+} ion numbers. Interestingly, it has been shown (52) that exactly the opposite is the case: namely, mobile buffers typically *increase* stochastic fluctuation amplitude. Therefore, another explanation for the close agreement between the two approaches is needed.

Our analysis of the simple two-compartment model suggests such an explanation. Namely, the inaccuracy of the deterministic description of FPTD is primarily determined by the correlations between fluctuations in the reactant molecule numbers, rather than the size of these fluctuations. This in turn follows from the fact that all reactions relevant to the Ca^{2+} buffering and sensing are *hetero-species* rather than *homo-species*: reactions occur between molecules of different types (59). In this case the mean-field description of the Ca^{2+} sensor approximates its stochastic description, under the simplifying assumption of zero correlations (cf. Eqs. 13-14). This correspondence would break down had Ca^{2+} sensing involved simultaneous binding of two Ca^{2+} ions to the exocytosis sensor, as opposed to a sequence of two binding reactions. This scenario would correspond to a larger ratio of between reaction and diffusion rates, which is expected to amplify the discrepancy between deterministic and stochastic approaches. These results are quite general and apply to the modeling of a wide class of biochemical cell processes. The significance of the relative magnitudes of reaction and diffusion rates have also been pointed out by prior studies (see e.g. (16,23,24,38,48)).

It is important to emphasize that the partial decorrelation between local Ca^{2+} fluctuations and the sensor state fluctuations does not imply a small uncertainty in FPT: in fact, FPTD is still quite “wide” (i.e. has a large variance) even in cases where the mean-field results achieve significant accuracy (see Figs. 1-2,S1-S2). We note that this finding is similar to, but somewhat distinct from the concept of stochastic shielding, whereby stochastic fluctuations of upstream reactions in a given biochemical pathway are effectively shielded from fluctuations of observable variables (such as open states of an ion channel), which are more sensitive to fluctuations in downstream parts of the pathway (113,114).

The above-mentioned threshold of N_{Ca}=50 inferred from our 3D simulations may seem to contradict our analysis of the reduced two-compartment model, which showed that good agreement between stochastic and deterministic (mean-field) estimates of FPTD can be achieved even for N_{Ca}~O(1). However, Fig. 3A shows that the local number of Ca^{2+} ions in the vicinity of the Ca^{2+} sensor, n, is much smaller than the total number of ions N_{Ca} in the full 3D simulation.

It should also be noted that independently varying the diffusion and reaction rates, as we did in Figs. 5-6 in the two-compartment model, would be conceptually problematic in the 3D model, since bi-molecular binding reactions are inherently limited by diffusion. Therefore, it would be useful to bridge the conceptual gap between compartmental and fully spatially resolved models, while retaining the ability for rigorous analysis. The most promising approach in this direction is to use recent simplified models of Ca^{2+} diffusion, buffering and binding that allow closed-form computation of FPTD (49-51). Although the latter studies involve certain simplifications, particularly in their reduced descriptions of Ca^{2+} buffering, it would be promising to examine the discrepancy between stochastic and deterministic FPTD obtained in the framework of such simplified models.

It is possible that part of the discrepancy between the mean-field and fully stochastic approaches could arise from the inherent difference in their treatment of bimolecular binding, as reviewed in Methods. However, we believe it is important to compare the most straightforward and easily implementable approaches, as we have done here, since these are most often used in practice. Further study may be needed to confirm whether the discrepancy between the two approaches is significantly affected by the differences in the Ca^{2+} sensor binding implementation. In general, single-molecule scale effects can only be precisely computed using exact event-based stochastic methods like FPKMC/GFRD (60,72-77), or more detailed molecular dynamics simulations (103).

Declaration of Interests

The author declares no competing interests.

Acknowledgements

The Author acknowledges useful discussions with A. Donev (NYU) and M.G. Pedersen (University of Padova). This work was supported in part by NSF grant DMS-1517085.

APPENDIX: CME system for the two-compartment model

Let $p_n^k(t)$ denote the probabilities of Markovian states in Eq. 12, corresponding to n (n=0..N) Ca^{2+} ions in the sensor sub-compartment while the sensor is in state S_k, k=0..3, with k=3 indexing the terminal fused (release) state R in the sensor binding reaction, Eq. 8. Then the Markov Chain shown in Eq. 12 corresponds to the following Chemical Master Equation (CME) system (Kolmogorov forward equations):

$$\begin{aligned}
\frac{dp_n^0}{dt} &= \alpha\left[(N-n+1)\,p_{n-1}^0-(N-n)\,p_n^0\right]+\beta\left[(n+1)\,p_{n+1}^0-np_n^0\right] \\
&\quad +k_1^-\,p_{n-1}^0-nk_1^+\,p_n^0 \quad (n=0\ldots N), \\
\frac{dp_n^1}{dt} &= \alpha\left[(N-n)\,p_{n-1}^1-(N-n-1)\,p_n^1\right]+\beta\left[(n+1)\,p_{n+1}^1-np_n^1\right] \\
&\quad +k_2^-\,p_{n-1}^2-nk_2^+\,p_n^2-k_1^-\,p_n^1+(n+1)k_1^+\,p_{n+1}^0 \quad (n=0\ldots N-1), \\
\frac{dp_n^2}{dt} &= \alpha\left[(N-n-1)\,p_{n-1}^2-(N-n-2)\,p_n^2\right]+\beta\left[(n+1)\,p_{n+1}^2-np_n^2\right] \\
&\quad -k_2^-\,p_n^2+(n+1)k_2^+\,p_{n+1}^1-\gamma\,p_n^2 \quad (n=0\ldots N-2), \\
\frac{dp_n^3}{dt} &= \alpha\left[(N-n-1)\,p_{n-1}^3-(N-n-2)\,p_n^3\right]+\beta\left[(n+1)\,p_{n+1}^3-np_n^3\right]+\gamma\,p_n^2 \quad (n=0\ldots N-2).
\end{aligned} \tag{15}$$

This is a linear system of form d**p**/dt = W**p**, where the components of probability vector **p** correspond to the 4N–1 states shown in Eq. 12, and the elements of Markov transition matrix W are constant rates indicated in Eqs. 12, 15. Therefore, it is readily integrated in closed-form: **p**(t) = exp[W t] **p**(0). Since our quantity of interest is FPTD, given by the rate of transition to the final absorbing (release) state R, all states (n, R) with probabilities $p_n^3(t)$ could be collapsed onto a single absorbing state by summing over n. Further, one more variable could be eliminated using the conservation law for the sum of all states of the sensor. However, we keep all states in Eqs. 12, 15, for the sake of clarity.

This CME system can be converted to an ODE system of the same dimensionality describing the moments of the state variables, i.e. the occupancy probabilities of sensor states $\langle S_k\rangle$ and $\langle R\rangle$, and the moments of n, which depend on the state of the sensor, and denoted as $\langle n^m, S_k\rangle$:

$$\begin{aligned}
&\left\langle S_k\right\rangle=\sum_{n=0}^{M_k}p_n^k(t), \quad k=0\ldots3, \\
&\left\langle n^m,\,S_k\right\rangle=\sum_{n=1}^{M_k}n^m\,p_n^k(t), \quad m=1,\ldots,M_k \\
&\left\langle n\right\rangle=\sum_{n=1}^{M_k}\sum_{k=0}^{3}n\,p_n^k(t),
\end{aligned} \tag{163}$$

where $M_k=N-\min(k,2)$ is the number of free (unbound) Ca^{2+} ions contained in both compartments when the sensor is in state k. Introducing conditional moments through the standard definition $\left\langle n^m,\,S_k\right\rangle=\left\langle n^m\mid S_k\right\rangle\left\langle S_k\right\rangle$, and performing appropriate summations of Eqs. 15 and algebraic simplifications, one obtains the moment system, part of which is shown in Eq. 13. The initial condition corresponding to Figs. 5, 6 is given by $p_0^0(0)=1$, with all other probabilities satisfying $p_n^k(0)=0$.

Supporting Material

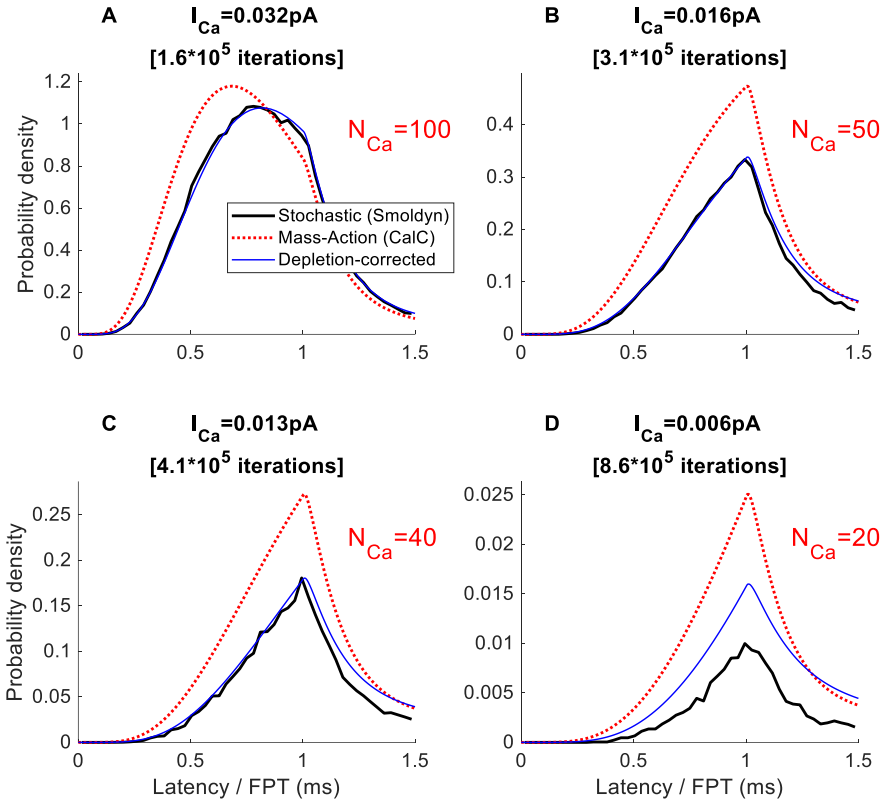

Figure S1. Mass-action vs stochastic simulation of FPTD for unphysiologically large sensor binding rate, and a greater distance between release sensor and the Ca^{2+} channel, in response to a 1ms-long Ca^{2+} current pulse of varying amplitude. Simulation parameters are similar to the ones in Figs. 1-2, except a factor of 10 faster exocytosis sensor binding rate k^+, requiring a smaller MC simulation time step of Δt=0.1μs, larger diffusion volume of $(0.3\mu m)^3$, and larger distance from channel to sensor of 83 nm. The Ca^{2+} current value and the total number of Ca^{2+} ions entering during the 1-ms long current pulse is indicated in the panel titles. In all panels, *black solid curves* represent the histograms of FPT to full sensor binding, the *dotted red* curves show the corresponding deterministic estimates of FPTD (Eq. 5), with binding depletion ignored (σ_S=0 in Eq.2), while the *solid blue* curves show the deterministic estimate of FPTD, with binding depletion taken into account (Eqs. 6-7). Note the difference in scale: the cumulative probability of binding within 1.5ms is about 74% in *A* (N_{Ca}=200), while in *D* (N_{Ca}=20) it is ~0.5%.

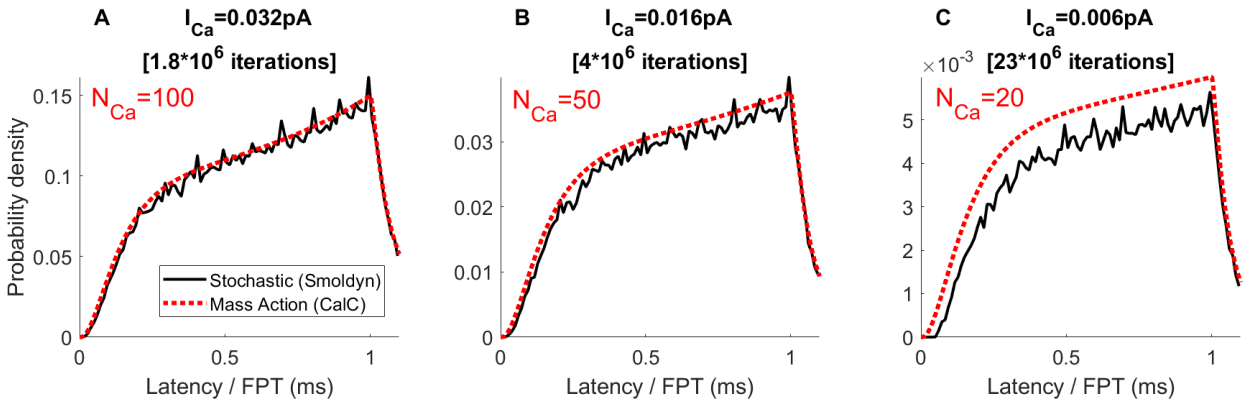

Figure S2. Mass-action vs stochastic simulation of FPTD for the case of Ca^{2+} sensor with only two Ca^{2+} binding sires, which bind Ca in a non-cooperative manner, so that the binding scheme is replaced with

$$S_0 \underset{k^-}{\overset{2k^+Ca}{\rightleftharpoons}} S_1 \underset{2k^-}{\overset{k^+Ca}{\rightleftharpoons}} S_2 \overset{\gamma}{\rightarrow} \mathbf{R}.$$

Other parameters are the same as in Fig. 2 and Eq. 3. The Ca^{2+} current value and the total number of Ca^{2+} ions entering during the 1-ms long current pulse is indicated in the panel titles. In all panels, *black solid curves* represent the histograms of FPT to full sensor binding, and the *dashed red* curves show the corresponding deterministic estimates of FPTD (Eq. 5). The depletion correction (shown as blue curves in Figs. 2 and S1) has only a negligible impact on FPTD for the parameter values used in this Figure, and therefore is not shown. Note the difference in vertical axis scale for the 3 panels.

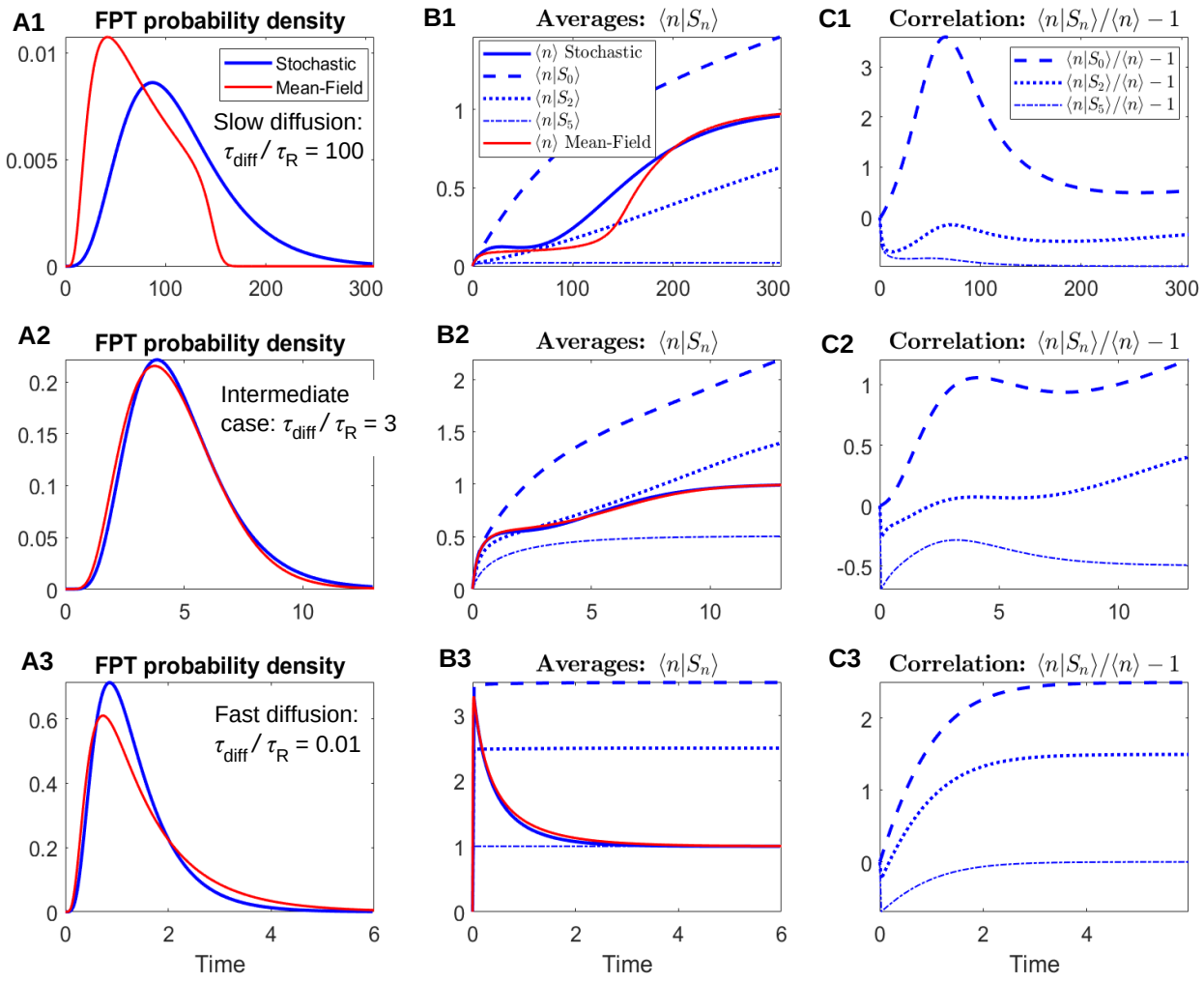

Figure S3. Comparison between mass-action and stochastic simulation of the two-compartment model as in Fig. 5, but for the case of a Ca^{2+} sensor with 5 biding sites, as in Eq. 3:

$$S_0 \underset{k^-}{\overset{5k^+Ca}{\rightleftharpoons}} S_1 \underset{2bk^-}{\overset{4k^+Ca}{\rightleftharpoons}} S_2 \underset{3b^2k^-}{\overset{3k^+Ca}{\rightleftharpoons}} S_3 \underset{4b^3k^-}{\overset{2k^+Ca}{\rightleftharpoons}} S_4 \underset{5b^4k^-}{\overset{k^+Ca}{\rightleftharpoons}} S_5 \overset{\gamma}{\rightarrow} \mathbf{R}.$$

Here $k^+ = k^- = 1,\ \gamma = 2, b = 0.25$. The total number of Ca^{2+} ions is **N=7**, so that only 2 ions remain free upon full sensor binding. The ratios between diffusion and reaction time scales are as in Fig. 5: τ_{diff}/τ_R=100 (**A1-C1**), τ_{diff}/τ_R=3 (**A2-C2**), and τ_{diff}/τ_R=0.01 (**A3-C3**). This ratio is controlled by varying the diffusion rate $\alpha = \beta = 1/\tau_{diff}$, while keeping reaction rates constant. (**A1**,**A2**,**A3**) First-passage time to full binding probability density (FPTD). (**B1**,**B2**,**B3**) Average number of Ca^{2+} ions in the sensor compartment. For the stochastic simulation, also shown are the average number of Ca^{2+} ions conditional on the sensor state, $\langle n_{Ca}|S_k\rangle$, for k=0 (dashed blue curve), k=2 (dotted blue curve), and k=5 (dashed-dotted blue curve). Note that the number of ions in the sensor compartment approaches n=1 in all cases, since the total number of Ca^{2+} ions is N=7. (**C1**,**C2**,**C3**) Correlation between the number of Ca^{2+} ions in the sensor compartment and the sensor state, given by the ratio of conditional and unconditional expectations $\langle n_{Ca}|S_k\rangle/\langle n_{Ca}\rangle$ (k=0,2,5).

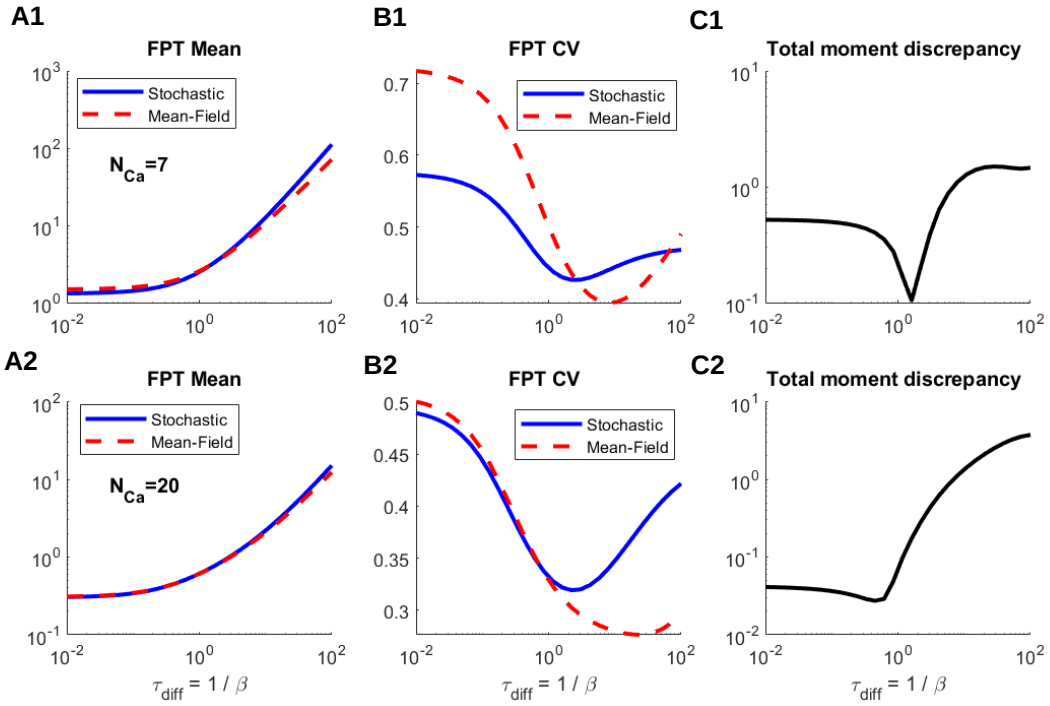

Figure S4. Comparison of the correlations and the central moments of FPTD obtained using deterministic mean-field vs. stochastic approaches, as a function of diffusive time constant $\tau_{diff} = 1/\beta$, for two values of total particle number, N=7 (A1-D1) and N=20 (A2-D2). This Figure repeats simulations in Fig. 6, but for a Ca^{2+} sensor that binds 5 Ca^{2+} ions in a cooperative manner, as in Eq. 3 and Fig. S3. (**A**1, **A2**): FPT average, (**B1**, **B2**): coefficient of variance of FPT, (**C1**, **C2**): total normalized discrepancy of first 3 central moments of FPTD between stochastic and deterministic simulations. Diffusive rates satisfy $\alpha/\beta=1$ for all simulation conditions, ensuring that the average number of ions in the sensor compartment after full sensor binding is n=1 in (A1-C1) and n=7.5 in (A2-C2).

REFERENCES

1. Augustine, G. J., F. Santamaria, and K. Tanaka. 2003. Local calcium signaling in neurons. *Neuron*. 40(2):331-346, doi: 10.1016/s0896-6273(03)00639-1, https://pubmed.ncbi.nlm.nih.gov/14556712/.

2. Konieczny, V., M. V. Keebler, and C. W. Taylor. 2012. Spatial organization of intracellular Ca2+ signals. *Semin Cell Dev Biol*. 23(2):172-180, doi: 10.1016/j.semcdb.2011.09.006, http://www.ncbi.nlm.nih.gov/pubmed/21925615.

3. Dupont, G., M. Falcke, V. Kirk, and J. Sneyd. 2016. Models of Calcium Signalling. Springer.

4. Stanley, E. F. 2016. The Nanophysiology of Fast Transmitter Release. *Trends Neurosci*. 39(3):183-197, doi: 10.1016/j.tins.2016.01.005, http://www.ncbi.nlm.nih.gov/pubmed/26896416.

5. Thurley, K., A. Skupin, R. Thul, and M. Falcke. 2012. Fundamental properties of Ca2+ signals. *Biochim Biophys Acta*. 1820(8):1185-1194, doi: 10.1016/j.bbagen.2011.10.007, http://www.ncbi.nlm.nih.gov/pubmed/22040723.

6. Dobrzynski, M., J. V. Rodriguez, J. A. Kaandorp, and J. G. Blom. 2007. Computational methods for diffusion-influenced biochemical reactions. *Bioinformatics*. 23(15):1969-1977, doi: 10.1093/bioinformatics/btm278, http://www.ncbi.nlm.nih.gov/pubmed/17537752.

7. Wieder, N., R. H. Fink, and F. Wegner. 2011. Exact and approximate stochastic simulation of intracellular calcium dynamics. *J Biomed Biotechnol*. 2011:572492, doi: 10.1155/2011/572492, http://www.ncbi.nlm.nih.gov/pubmed/22131814.

8. Gillespie, D. T., A. Hellander, and L. R. Petzold. 2013. Perspective: Stochastic algorithms for chemical kinetics. *J Chem Phys*. 138(17):170901, doi: 10.1063/1.4801941, https://www.ncbi.nlm.nih.gov/pubmed/23656106.

9. Blackwell, K. T. 2013. Approaches and tools for modeling signaling pathways and calcium dynamics in neurons. *J Neurosci Methods*. 220(2):131-140, doi: 10.1016/j.jneumeth.2013.05.008, http://www.ncbi.nlm.nih.gov/pubmed/23743449.

10. Maleckar, M. M., A. G. Edwards, W. E. Louch, and G. T. Lines. 2017. Studying dyadic structure-function relationships: a review of current modeling approaches and new insights into Ca(2+) (mis)handling. *Clin Med Insights Cardiol*. 11:1179546817698602, doi: 10.1177/1179546817698602, https://www.ncbi.nlm.nih.gov/pubmed/28469494.

11. Neher, E. 1998. Vesicle pools and Ca2+ microdomains: new tools for understanding their roles in neurotransmitter release. *Neuron*. 20(3):389-399, https://pubmed.ncbi.nlm.nih.gov/9539117/.

12. Matthews, E. A., and D. Dietrich. 2015. Buffer mobility and the regulation of neuronal calcium domains. *Front Cell Neurosci*. 9:48, doi: 10.3389/fncel.2015.00048, http://www.ncbi.nlm.nih.gov/pubmed/25750615.

13. Guerrier, C., and D. Holcman. 2018. The First 100 nm Inside the Pre-synaptic Terminal Where Calcium Diffusion Triggers Vesicular Release. *Front Synaptic Neurosci*. 10:23, doi: 10.3389/fnsyn.2018.00023, http://www.ncbi.nlm.nih.gov/pubmed/30083101.

14. Guerrier, C., and D. Holcman. 2016. Hybrid Markov-mass action law model for cell activation by rare binding events: Application to calcium induced vesicular release at neuronal synapses. *Sci Rep*. 6:35506, doi: 10.1038/srep35506, http://www.ncbi.nlm.nih.gov/pubmed/27752087.

15. Bhalla, U. S. 2004. Signaling in small subcellular volumes. II. Stochastic and diffusion effects on synaptic network properties. *Biophys J*. 87(2):745-753, doi: 10.1529/biophysj.104.040501, https://www.ncbi.nlm.nih.gov/pubmed/15298883.

16. Bhalla, U. S. 2004. Signaling in small subcellular volumes. I. Stochastic and diffusion effects on individual pathways. *Biophys J*. 87(2):733-744, doi: 10.1529/biophysj.104.040469, https://www.ncbi.nlm.nih.gov/pubmed/15298882.

17. De Schutter, E. 2013. The importance of stochastic signaling processes in the induction of long-term synaptic plasticity. *Neural Netw*. 47:3-10, doi: 10.1016/j.neunet.2012.11.015, https://www.ncbi.nlm.nih.gov/pubmed/23267752.

18. Pablo, M., S. A. Ramirez, and T. C. Elston. 2018. Particle-based simulations of polarity establishment reveal stochastic promotion of Turing pattern formation. *PLoS Comput Biol*. 14(3):e1006016, doi: 10.1371/journal.pcbi.1006016, https://www.ncbi.nlm.nih.gov/pubmed/29529021.

19. Falcke, M. 2003. On the role of stochastic channel behavior in intracellular Ca2+ dynamics. *Biophys J*. 84(1):42-56, doi: 10.1016/S0006-3495(03)74831-0, http://www.ncbi.nlm.nih.gov/pubmed/12524264.

20. Falcke, M. 2004. Reading patterns in living cells - the physics of Ca2+ signaling. *Advances in Physics*. 53(3):154, doi: 10.1080/00018730410001703159, https://www.tandfonline.com/doi/abs/10.1080/00018730410001703159.

21. Thul, R. F., M. 2004. Stability of membrane bound reactions. *Physical Review Letters*. 93, doi: 10.1103/PhysRevLett.93.188103, https://pubmed.ncbi.nlm.nih.gov/15525212/.

22. Diambra, L., and N. Guisoni. 2005. Modeling stochastic Ca2+ release from a cluster of IP3-sensitive receptors. *Cell Calcium*. 37(4):321-332, doi: 10.1016/j.ceca.2004.12.001, https://www.ncbi.nlm.nih.gov/pubmed/15755493.

23. Tanskanen, A. J., J. L. Greenstein, A. Chen, S. X. Sun, and R. L. Winslow. 2007. Protein geometry and placement in the cardiac dyad influence macroscopic properties of calcium-induced calcium release. *Biophys J*. 92(10):3379-3396, doi: 10.1529/biophysj.106.089425, http://www.ncbi.nlm.nih.gov/pubmed/17325016.

24. Hake, J., and G. T. Lines. 2008. Stochastic binding of Ca2+ ions in the dyadic cleft; continuous versus random walk description of diffusion. *Biophys J*. 94(11):4184-4201, doi: 10.1529/biophysj.106.103523, http://www.ncbi.nlm.nih.gov/pubmed/18263662.

25. Solovey, G., D. Fraiman, and S. P. Dawson. 2011. Mean field strategies induce unrealistic non-linearities in calcium puffs. *Front Physiol*. 2:46, doi: 10.3389/fphys.2011.00046, http://www.ncbi.nlm.nih.gov/pubmed/21869877.

26. Weinberg, S. H., and G. D. Smith. 2012. Discrete-state stochastic models of calcium-regulated calcium influx and subspace dynamics are not well-approximated by ODEs that neglect concentration fluctuations. *Comput Math Methods Med*. 2012:897371, doi: 10.1155/2012/897371, http://www.ncbi.nlm.nih.gov/pubmed/23509597.

27. Flegg, M. B., S. Rudiger, and R. Erban. 2013. Diffusive spatio-temporal noise in a first-passage time model for intracellular calcium release. *J Chem Phys*. 138(15):154103, doi: 10.1063/1.4796417, http://www.ncbi.nlm.nih.gov/pubmed/23614408.

28. Wieder, N., R. Fink, and F. von Wegner. 2015. Exact stochastic simulation of a calcium microdomain reveals the impact of Ca(2)(+) fluctuations on IP(3)R gating. *Biophys J*. 108(3):557-567, doi: 10.1016/j.bpj.2014.11.3458, http://www.ncbi.nlm.nih.gov/pubmed/25650923.

29. Modchang, C., S. Nadkarni, T. M. Bartol, W. Triampo, T. J. Sejnowski, H. Levine, and W. J. Rappel. 2010. A comparison of deterministic and stochastic simulations of neuronal vesicle release models. *Phys Biol*. 7(2):026008, doi: 10.1088/1478-3975/7/2/026008, http://www.ncbi.nlm.nih.gov/pubmed/20505227.

30. Schaff, J. C., F. Gao, Y. Li, I. L. Novak, and B. M. Slepchenko. 2016. Numerical Approach to Spatial Deterministic-Stochastic Models Arising in Cell Biology. *PLoS Comput Biol*. 12(12):e1005236, doi: 10.1371/journal.pcbi.1005236, https://www.ncbi.nlm.nih.gov/pubmed/27959915.

31. Swillens, S., P. Champeil, L. Combettes, and G. Dupont. 1998. Stochastic simulation of a single inositol 1,4,5-trisphosphate-sensitive Ca2+ channel reveals repetitive openings during 'blip-like' Ca2+ transients. *Cell Calcium*. 23(5):291-302, doi: 10.1016/s0143-4160(98)90025-2, https://www.ncbi.nlm.nih.gov/pubmed/9681192.

32. Thul, R., and M. Falcke. 2005. Reactive clusters on a membrane. *Phys Biol*. 2(1):51-59, doi: 10.1088/1478-3967/2/1/007, http://www.ncbi.nlm.nih.gov/pubmed/16204857.

33. Nguyen, V., R. Mathias, and G. D. Smith. 2005. A stochastic automata network descriptor for Markov chain models of instantaneously coupled intracellular Ca2+ channels. *Bull Math Biol*. 67(3):393-432, doi: 10.1016/j.bulm.2004.08.010, http://www.ncbi.nlm.nih.gov/pubmed/15820736.

34. Izu, L. T., S. A. Means, J. N. Shadid, Y. Chen-Izu, and C. W. Balke. 2006. Interplay of ryanodine receptor distribution and calcium dynamics. *Biophys J*. 91(1):95-112, doi: 10.1529/biophysj.105.077214, https://www.ncbi.nlm.nih.gov/pubmed/16603499.

35. Means, S., A. J. Smith, J. Shepherd, J. Shadid, J. Fowler, R. J. Wojcikiewicz, T. Mazel, G. D. Smith, and B. S. Wilson. 2006. Reaction diffusion modeling of calcium dynamics with realistic ER geometry. *Biophys J*. 91(2):537-557, doi: 10.1529/biophysj.105.075036, https://www.ncbi.nlm.nih.gov/pubmed/16617072.

36. Rudiger, S., J. W. Shuai, W. Huisinga, C. Nagaiah, G. Warnecke, I. Parker, and M. Falcke. 2007. Hybrid stochastic and deterministic simulations of calcium blips. *Biophys J*. 93(6):1847-1857, doi: 10.1529/biophysj.106.099879, http://www.ncbi.nlm.nih.gov/pubmed/17496042.

37. Solovey, G., D. Fraiman, B. Pando, and S. Ponce Dawson. 2008. Simplified model of cytosolic Ca2+ dynamics in the presence of one or several clusters of Ca2+ -release channels. *Phys Rev E Stat Nonlin Soft Matter Phys*. 78(4 Pt 1):041915, doi: 10.1103/PhysRevE.78.041915, https://www.ncbi.nlm.nih.gov/pubmed/18999463.

38. Shuai, J., J. E. Pearson, and I. Parker. 2008. Modeling Ca2+ feedback on a single inositol 1,4,5-trisphosphate receptor and its modulation by Ca2+ buffers. *Biophys J*. 95(8):3738-3752, doi: 10.1529/biophysj.108.137182, https://www.ncbi.nlm.nih.gov/pubmed/18641077.

39. Skupin, A., H. Kettenmann, and M. Falcke. 2010. Calcium signals driven by single channel noise. *PLoS Comput Biol*. 6(8), doi: 10.1371/journal.pcbi.1000870, https://www.ncbi.nlm.nih.gov/pubmed/20700497.

40. Montefusco, F., and M. G. Pedersen. 2018. Explicit Theoretical Analysis of How the Rate of Exocytosis Depends on Local Control by Ca(2+) Channels. *Comput Math Methods Med*. 2018:5721097, doi: 10.1155/2018/5721097, http://www.ncbi.nlm.nih.gov/pubmed/30607171.

41. Kobbersmed, J. R., A. T. Grasskamp, M. Jusyte, M. A. Bohme, S. Ditlevsen, J. B. Sorensen, and A. M. Walter. 2020. Rapid regulation of vesicle priming explains synaptic facilitation despite heterogeneous vesicle:Ca(2+) channel distances. *Elife*. 9, doi: 10.7554/eLife.51032, https://www.ncbi.nlm.nih.gov/pubmed/32077852.

42. Anwar, H., I. Hepburn, H. Nedelescu, W. Chen, and E. De Schutter. 2013. Stochastic calcium mechanisms cause dendritic calcium spike variability. *J Neurosci*. 33(40):15848-15867, doi: 10.1523/JNEUROSCI.1722-13.2013, https://www.ncbi.nlm.nih.gov/pubmed/24089492.

43. Stanley, D. A., B. L. Bardakjian, M. L. Spano, and W. L. Ditto. 2011. Stochastic amplification of calcium-activated potassium currents in Ca2+ microdomains. *J Comput Neurosci*. 31(3):647-666, doi: 10.1007/s10827-011-0328-x, https://www.ncbi.nlm.nih.gov/pubmed/21538141.

44. Erban, R., J. Chapman, and P. Maini. 2007. A practical guide to stochastic simulations of reaction-diffusion processes. 0704.1908, doi: 10.48550/arXiv.0704.1908, https://arxiv.org/abs/0704.1908.

45. Erban, R., and S. J. Chapman. 2020. Stochastic Modelling of Reaction-Diffusion Processes. Cambridge University Press, Cambridge, UK.

46. Guerrier, G., and D. Holcman. 2014. Brownian search for targets hidden in cusp-like pockets: Progress and Applications. *The European Physical Journal Special Topics*. 223(14):13, doi: 10.1140/epjst/e2014-02332-6, https://link.springer.com/article/10.1140/epjst/e2014-02332-6.

47. Guerrier, C., and D. Holcman. 2015. Search Time for a Small Ribbon and Application to Vesicular Release at Neuronal Synapses. *Multiscale Model. Simul.* 13(4):21, doi: 10.1137/15M1009512, https://epubs.siam.org/doi/abs/10.1137/15M1009512.

48. Weinberg, S. H. 2016. Microdomain [Ca(2+)] Fluctuations Alter Temporal Dynamics in Models of Ca(2+)-Dependent Signaling Cascades and Synaptic Vesicle Release. *Neural Comput*. 28(3):493-524, doi: 10.1162/NECO_a_00811, http://www.ncbi.nlm.nih.gov/pubmed/26735745.

49. Grebenkov, D. S. 2017. First passage times for multiple particles with reversible target-binding kinetics. *J Chem Phys*. 147(13):134112, doi: 10.1063/1.4996395, https://www.ncbi.nlm.nih.gov/pubmed/28987086.

50. Reva, M., D. A. DiGregorio, and D. S. Grebenkov. 2021. A first-passage approach to diffusion-influenced reversible binding and its insights into nanoscale signaling at the presynapse. *Sci Rep*. 11(1):5377, doi: 10.1038/s41598-021-84340-4, https://www.ncbi.nlm.nih.gov/pubmed/33686123.

51. Lawley, S. D., and J. B. Madrid. 2019. First passage time distribution of multiple impatient particles with reversible binding. *J Chem Phys*. 150(21):214113, doi: 10.1063/1.5098312, https://www.ncbi.nlm.nih.gov/pubmed/31176340.

52. Weinberg, S. H., and G. D. Smith. 2014. The influence of Ca(2)(+) buffers on free [Ca(2)(+)] fluctuations and the effective volume of Ca(2)(+) microdomains. *Biophys J*. 106(12):2693-2709, doi: 10.1016/j.bpj.2014.04.045, http://www.ncbi.nlm.nih.gov/pubmed/24940787.

53. Smith, G. D., J. Wagner, and J. Keizer. 1996. Validity of the rapid buffering approximation near a point source of calcium ions. *Biophys J*. 70(6):2527-2539, doi: 10.1016/S0006-3495(96)79824-7, http://www.ncbi.nlm.nih.gov/pubmed/8744292.

54. Smith, G. D., L. X. Dai, R. M. Miura, and A. Sherman. 2001. Asymptotic analysis of buffered calcium diffusion near a point source. *SIAM Journal on Applied Mathematics*. 61(5):1816-1838, https://www.jstor.org/stable/3061854.

55. Chen, Y., C. B. Muratov, and V. Matveev. 2020. Efficient Approximations for Stationary Single-Channel Ca(2+) Nanodomains across Length Scales. *Biophys J*. 119(6):1239-1254, doi: 10.1016/j.bpj.2020.06.038, https://www.ncbi.nlm.nih.gov/pubmed/32877663.

56. Schneggenburger, R., and E. Neher. 2000. Intracellular calcium dependence of transmitter release rates at a fast central synapse. *Nature*. 406(6798):889-893, doi: 10.1038/35022702, http://www.ncbi.nlm.nih.gov/entrez/query.fcgi?cmd=Retrieve&db=PubMed&dopt=Citation&list_uids=10972290.

57. Felmy, F., E. Neher, and R. Schneggenburger. 2003. Probing the intracellular calcium sensitivity of transmitter release during synaptic facilitation. *Neuron*. 37(5):801-811, doi: 10.1016/s0896-6273(03)00085-0, https://pubmed.ncbi.nlm.nih.gov/12628170/.

58. Gardiner, C. 2009. Stochastic Methods: A Handbook for the Natural and Social Sciences. Springer-Verlag, Berlin Heidelberg.

59. Erban, R., and S. J. Chapman. 2009. Stochastic modelling of reaction-diffusion processes: algorithms for bimolecular reactions. *Phys Biol*. 6(4):046001, doi: 10.1088/1478-3975/6/4/046001, http://www.ncbi.nlm.nih.gov/pubmed/19700812.

60. Donev, A. Y., C.-Y.; Kim, C. 2018. Efficient Reactive Brownian Dynamics. *Journal of Chemical Physics*. 148:16, doi: 10.1063/1.5009464, https://aip.scitation.org/doi/10.1063/1.5009464.

61. Kits, K. S., T. A. de Vlieger, B. W. Kooi, and H. D. Mansvelder. 1999. Diffusion barriers limit the effect of mobile calcium buffers on exocytosis of large dense cored vesicles. *Biophys J*. 76(3):1693-1705, doi: 10.1016/S0006-3495(99)77328-5, https://pubmed.ncbi.nlm.nih.gov/10049349/.

62. Segura, J., A. Gil, and B. Soria. 2000. Modeling study of exocytosis in neuroendocrine cells: influence of the geometrical parameters. *Biophys J*. 79(4):1771-1786, doi: 10.1016/S0006-3495(00)76429-0, http://www.ncbi.nlm.nih.gov/pubmed/11023885.

63. Glavinovic, M. I., and H. R. Rabie. 2001. Monte Carlo evaluation of quantal analysis in the light of Ca2+ dynamics and the geometry of secretion. *Pflugers Arch*. 443(1):132-145, doi: 10.1007/s004240100631, https://pubmed.ncbi.nlm.nih.gov/11692277/.

64. Shahrezaei, V., and K. R. Delaney. 2004. Consequences of molecular-level Ca2+ channel and synaptic vesicle colocalization for the Ca2+ microdomain and neurotransmitter exocytosis: a monte carlo study. *Biophys J*. 87(4):2352-2364, doi: 10.1529/biophysj.104.043380, https://pubmed.ncbi.nlm.nih.gov/15454435/.

65. Graydon, C. W., S. Cho, G. L. Li, B. Kachar, and H. von Gersdorff. 2011. Sharp Ca(2)(+) nanodomains beneath the ribbon promote highly synchronous multivesicular release at hair cell synapses. *J Neurosci*. 31(46):16637-16650, doi: 10.1523/JNEUROSCI.1866-11.2011, http://www.ncbi.nlm.nih.gov/pubmed/22090491.

66. Biess, A., E. Korkotian, and D. Holcman. 2011. Barriers to diffusion in dendrites and estimation of calcium spread following synaptic inputs. *PLoS Comput Biol*. 7(10):e1002182, doi: 10.1371/journal.pcbi.1002182, http://www.ncbi.nlm.nih.gov/pubmed/22022241.

67. Matveev, V., A. Sherman, and R. S. Zucker. 2002. New and corrected simulations of synaptic facilitation. *Biophys J*. 83(3):1368-1373, doi: 10.1016/S0006-3495(02)73907-6, https://www.ncbi.nlm.nih.gov/pmc/articles/PMC1302235/.

68. Matveev, V. 2021. http://www.calciumcalculator.org

69. Agbanusi, I. C., and S. A. Isaacson. 2014. A comparison of bimolecular reaction models for stochastic reaction-diffusion systems. *Bull Math Biol*. 76(4):922-946, doi: 10.1007/s11538-013-9833-6, https://www.ncbi.nlm.nih.gov/pubmed/23579988.

70. Rudiger, S. 2014. Stochastic models of intracellular calcium signals. *Physics Reports*. 534:39-87, doi: 10.1016/j.physrep.2013.09.002, https://www.sciencedirect.com/science/article/abs/pii/S0370157313003463.

71. Kang, H. W., and R. Erban. 2019. Multiscale Stochastic Reaction-Diffusion Algorithms Combining Markov Chain Models with Stochastic Partial Differential Equations. *Bull Math Biol*. 81(8):3185-3213, doi: 10.1007/s11538-019-00613-0, https://www.ncbi.nlm.nih.gov/pubmed/31165406.

72. Oppelstrup, T., V. V. Bulatov, G. H. Gilmer, M. H. Kalos, and B. Sadigh. 2006. First-passage Monte Carlo algorithm: diffusion without all the hops. *Phys Rev Lett*. 97(23):230602, http://www.ncbi.nlm.nih.gov/pubmed/17280187.

73. Oppelstrup, T., V. V. Bulatov, A. Donev, M. H. Kalos, G. H. Gilmer, and B. Sadigh. 2009. First-passage kinetic Monte Carlo method. *Phys Rev E Stat Nonlin Soft Matter Phys*. 80(6 Pt 2):066701, doi: 10.1103/PhysRevE.80.066701, http://www.ncbi.nlm.nih.gov/pubmed/20365296.

74. Donev, A., V. V. Bulatov, T. Oppelstrup, G. H. Gilmer, B. Sadigh, and M. H. Kalos. 2010. A First-Passage Kinetic Monte Carlo Algorithm for Complex Diffusion-Reaction Systems. *Journal of Computational Physics*. 229(9):25, doi: 10.1016/j.jcp.2009.12.038, https://dl.acm.org/doi/abs/10.1016/j.jcp.2009.12.038.

75. van Zon, J. S., and P. R. ten Wolde. 2005. Simulating biochemical networks at the particle level and in time and space: Green's function reaction dynamics. *Phys Rev Lett*. 94(12):128103, http://www.ncbi.nlm.nih.gov/pubmed/15903966.

76. van Zon, J. S., and P. R. ten Wolde. 2005. Green's-function reaction dynamics: a particle-based approach for simulating biochemical networks in time and space. *J Chem Phys*. 123(23):234910, doi: 10.1063/1.2137716, http://www.ncbi.nlm.nih.gov/pubmed/16392952.

77. Byrne, M. J., M. N. Waxham, and Y. Kubota. 2010. Cellular dynamic simulator: an event driven molecular simulation environment for cellular physiology. *Neuroinformatics*. 8(2):63-82, doi: 10.1007/s12021-010-9066-x, http://www.ncbi.nlm.nih.gov/pubmed/20361275.

78. Andrews, S. S., and D. Bray. 2004. Stochastic simulation of chemical reactions with spatial resolution and single molecule detail. *Phys Biol*. 1(3-4):137-151, doi: 10.1088/1478-3967/1/3/001, http://www.ncbi.nlm.nih.gov/pubmed/16204833.

79. Kerr, R. A., T. M. Bartol, B. Kaminsky, M. Dittrich, J. C. Chang, S. B. Baden, T. J. Sejnowski, and J. R. Stiles. 2008. Fast Monte Carlo Simulation Methods for Biological Reaction-Diffusion Systems

in Solution and on Surfaces. *SIAM Journal on Scientific Computing*. 30(6):3126, doi: 10.1137/070692017, http://www.ncbi.nlm.nih.gov/pubmed/20151023.

80. Boulianne, L., S. Al Assaad, M. Dumontier, and W. J. Gross. 2008. GridCell: a stochastic particle-based biological system simulator. *BMC Syst Biol*. 2:66, doi: 10.1186/1752-0509-2-66, http://www.ncbi.nlm.nih.gov/pubmed/18651956.

81. Ander, M., P. Beltrao, B. Di Ventura, J. Ferkinghoff-Borg, M. Foglierini, A. Kaplan, C. Lemerle, I. Tomas-Oliveira, and L. Serrano. 2004. SmartCell, a framework to simulate cellular processes that combines stochastic approximation with diffusion and localisation: analysis of simple networks. *Syst Biol (Stevenage)*. 1(1):129-138, http://www.ncbi.nlm.nih.gov/pubmed/17052123.

82. Hattne, J., D. Fange, and J. Elf. 2005. Stochastic reaction-diffusion simulation with MesoRD. *Bioinformatics*. 21(12):2923-2924, doi: 10.1093/bioinformatics/bti431, http://www.ncbi.nlm.nih.gov/pubmed/15817692.

83. Engblom, S., L. Ferm, A. Hellander, and P. Lotstedt. 2009. Simulation of stochastic reaction-diffusion processes on unstructured meshes. *SIAM Journal on Scientific Computing*. 31:24, doi: 10.1137/080721388, https://epubs.siam.org/doi/abs/10.1137/080721388.

84. Hepburn, I., W. Chen, S. Wils, and E. De Schutter. 2012. STEPS: efficient simulation of stochastic reaction-diffusion models in realistic morphologies. *BMC Syst Biol*. 6:36, doi: 10.1186/1752-0509-6-36, http://www.ncbi.nlm.nih.gov/pubmed/22574658.

85. Roberts, E., J. E. Stone, and Z. Luthey-Schulten. 2013. Lattice Microbes: high-performance stochastic simulation method for the reaction-diffusion master equation. *J Comput Chem*. 34(3):245-255, doi: 10.1002/jcc.23130, http://www.ncbi.nlm.nih.gov/pubmed/23007888.

86. Gillespie, D. T. 1976. A General Method for Numerically Simulating the Stochastic Time Evolution of Coupled Chemical Reactions. *Journal of Computational Physics*. 22:32, doi: 10.1016/0021-9991(76)90041-3, https://www.sciencedirect.com/science/article/pii/0021999176900413.

87. Isaacson, S. A. 2009. The Reaction-Diffusion Master Equation as an Asymptotic Approximation of Diffusion to a Small Target. *SIAM Journal on Applied Mathematics*. 70(1):35, doi: doi.org/10.1137/070705039, https://epubs.siam.org/doi/10.1137/070705039.

88. Fange, D., O. G. Berg, P. Sjoberg, and J. Elf. 2010. Stochastic reaction-diffusion kinetics in the microscopic limit. *Proc Natl Acad Sci U S A*. 107(46):19820-19825, doi: 10.1073/pnas.1006565107, https://www.ncbi.nlm.nih.gov/pubmed/21041672.

89. Hellander, S., A. Hellander, and L. Petzold. 2015. Reaction rates for mesoscopic reaction-diffusion kinetics. *Phys Rev E Stat Nonlin Soft Matter Phys*. 91(2):023312, doi: 10.1103/PhysRevE.91.023312, https://www.ncbi.nlm.nih.gov/pubmed/25768640.

90. Isaacson, S. A. 2013. A convergent reaction-diffusion master equation. *J Chem Phys*. 139(5):054101, doi: 10.1063/1.4816377, http://www.ncbi.nlm.nih.gov/pubmed/23927237.

91. Flegg, M. B., S. J. Chapman, and R. Erban. 2012. The two-regime method for optimizing stochastic reaction-diffusion simulations. *J R Soc Interface*. 9(70):859-868, doi: 10.1098/rsif.2011.0574, http://www.ncbi.nlm.nih.gov/pubmed/22012973.

92. Robinson, M., M. Flegg, and R. Erban. 2014. Adaptive two-regime method: application to front propagation. *J Chem Phys*. 140(12):124109, doi: 10.1063/1.4868652, http://www.ncbi.nlm.nih.gov/pubmed/24697426.

93. Wylie, D. C., Y. Hori, A. R. Dinner, and A. K. Chakraborty. 2006. A hybrid deterministic-stochastic algorithm for modeling cell signaling dynamics in spatially inhomogeneous environments and under the influence of external fields. *J Phys Chem B*. 110(25):12749-12765, doi: 10.1021/jp056231f, https://www.ncbi.nlm.nih.gov/pubmed/16800611.

94. Chiam, K. H., C. M. Tan, V. Bhargava, and G. Rajagopal. 2006. Hybrid simulations of stochastic reaction-diffusion processes for modeling intracellular signaling pathways. *Phys Rev E Stat Nonlin*

Soft Matter Phys. 74(5 Pt 1):051910, doi: 10.1103/PhysRevE.74.051910, https://www.ncbi.nlm.nih.gov/pubmed/17279942.

95. Rossinelli, D., B. Bayati, and P. Koumoutsakos. 2008. Accelerated stochastic and hybrid methods for spatial simulations of reaction–diffusion systems. *Chemical Physics Letters*. 451:5.

96. Kalantzis, G. 2009. Hybrid stochastic simulations of intracellular reaction-diffusion systems. *Comput Biol Chem*. 33(3):205-215, doi: 10.1016/j.compbiolchem.2009.03.002, https://www.ncbi.nlm.nih.gov/pubmed/19414282.

97. Franz, B., M. B. Flegg, S. J. Chapman, and R. Erban. 2013. Multiscale reaction-diffusion algorithms: PDE-assisted Brownian dynamics. *SIAM Journal on Applied Mathematics*. 73(3):24, https://www.jstor.org/stable/23479972.

98. Lo, W. C., L. Zheng, and Q. Nie. 2016. A hybrid continuous-discrete method for stochastic reaction-diffusion processes. *R Soc Open Sci*. 3(9):160485, doi: 10.1098/rsos.160485, https://www.ncbi.nlm.nih.gov/pubmed/27703710.

99. Bhattacharjee, A. K., K. Balakrishnan, A. L. Garcia, J. B. Bell, and A. Donev. 2015. Fluctuating hydrodynamics of multi-species reactive mixtures. *J Chem Phys*. 142(22):224107, doi: 10.1063/1.4922308, https://www.ncbi.nlm.nih.gov/pubmed/26071701.

100. Ghosh, A., A. Leier, and T. T. Marquez-Lago. 2015. The Spatial Chemical Langevin Equation and Reaction Diffusion Master Equations: moments and qualitative solutions. *Theor Biol Med Model*. 12:5, doi: 10.1186/s12976-015-0001-6, https://www.ncbi.nlm.nih.gov/pubmed/25888773.

101. Kim, C., A. Nonaka, J. B. Bell, A. L. Garcia, and A. Donev. 2017. Stochastic simulation of reaction-diffusion systems: A fluctuating-hydrodynamics approach. *J Chem Phys*. 146(12):124110, doi: 10.1063/1.4978775, https://www.ncbi.nlm.nih.gov/pubmed/28388111.

102. Lipková, J., K. C. Zygalakis, S. J. Chapman, and R. Erban. 2011. Analysis of Brownian Dynamics Simulations of Reversible Bimolecular Reactions. *SIAM Journal on Applied Mathematics*. 71(3):17, doi: 10.1137/100794213, https://epubs.siam.org/doi/10.1137/100794213.

103. Huber, G. A., and J. A. McCammon. 2019. Brownian Dynamics Simulations of Biological Molecules. *Trends Chem*. 1(8):727-738, doi: 10.1016/j.trechm.2019.07.008, https://www.ncbi.nlm.nih.gov/pubmed/32309795.

104. Ramirez, S. A., M. Pablo, S. Burk, D. J. Lew, and T. C. Elston. 2021. A novel stochastic simulation approach enables exploration of mechanisms for regulating polarity site movement. *PLoS Comput Biol*. 17(7):e1008525, doi: 10.1371/journal.pcbi.1008525, https://www.ncbi.nlm.nih.gov/pubmed/34264926.

105. Winkler, A. A., and E. Frey. 2013. Long-range and many-body effects in coagulation processes. *Phys Rev E Stat Nonlin Soft Matter Phys*. 87(2):022136, doi: 10.1103/PhysRevE.87.022136, https://www.ncbi.nlm.nih.gov/pubmed/23496488.

106. Winkler, A. A., and E. Frey. 2012. Validity of the law of mass action in three-dimensional coagulation processes. *Phys Rev Lett*. 108(10):108301, doi: 10.1103/PhysRevLett.108.108301, https://www.ncbi.nlm.nih.gov/pubmed/22463460.

107. Shuai, J. W., and P. Jung. 2002. Stochastic properties of Ca(2+) release of inositol 1,4,5-trisphosphate receptor clusters. *Biophys J*. 83(1):87-97, doi: 10.1016/S0006-3495(02)75151-5, https://www.ncbi.nlm.nih.gov/pubmed/12080102.

108. Dolphin, A. C. 2021. Functions of Presynaptic Voltage-gated Calcium Channels. *Function (Oxf)*. 2(1):zqaa027, doi: 10.1093/function/zqaa027, https://www.ncbi.nlm.nih.gov/pubmed/33313507.

109. Karagas, N. E., and K. Venkatachalam. 2019. Roles for the Endoplasmic Reticulum in Regulation of Neuronal Calcium Homeostasis. *Cells*. 8(10), doi: 10.3390/cells8101232, https://www.ncbi.nlm.nih.gov/pubmed/31658749.

110. Topolnik, L., and O. Camire. 2019. Non-linear calcium signalling and synaptic plasticity in interneurons. *Curr Opin Neurobiol*. 54:98-103, doi: 10.1016/j.conb.2018.09.006, https://www.ncbi.nlm.nih.gov/pubmed/30321867.

111. Singh, N., T. Bartol, H. Levine, T. Sejnowski, and S. Nadkarni. 2021. Presynaptic endoplasmic reticulum regulates short-term plasticity in hippocampal synapses. *Commun Biol*. 4(1):241, doi: 10.1038/s42003-021-01761-7, https://www.ncbi.nlm.nih.gov/pubmed/33623091.

112. Tran, V., and C. Stricker. 2021. Spontaneous and action potential-evoked Ca(2+) release from endoplasmic reticulum in neocortical synaptic boutons. *Cell Calcium*. 97:102433, doi: 10.1016/j.ceca.2021.102433, https://www.ncbi.nlm.nih.gov/pubmed/34174726.

113. Schmidt, D. R., and P. J. Thomas. 2014. Measuring edge importance: a quantitative analysis of the stochastic shielding approximation for random processes on graphs. *J Math Neurosci*. 4(1):6, doi: 10.1186/2190-8567-4-6, https://www.ncbi.nlm.nih.gov/pubmed/24742077.

114. Schmidt, D. R., R. F. Galan, and P. J. Thomas. 2018. Stochastic shielding and edge importance for Markov chains with timescale separation. *PLoS Comput Biol*. 14(6):e1006206, doi: 10.1371/journal.pcbi.1006206, https://www.ncbi.nlm.nih.gov/pubmed/29912862.